SANDIA REPORT

SAND2015-20782
Unlimited Release
Printed January, 2015

An Attempt to Calibrate and Validate a Simple Ductile Failure Model Against Axial-Torsion Experiments on Al 6061-T651

Benjamin Reedlunn, Wei-Yang Lu

Prepared by
Sandia National Laboratories
Albuquerque, New Mexico 87185 and Livermore, California 94550

Sandia National Laboratories is a multi-program laboratory managed and operated by Sandia Corporation, a wholly owned subsidiary of Lockheed Martin Corporation, for the U.S. Department of Energy's National Nuclear Security Administration under contract DE-AC04-94AL85000.

Sandia National Laboratories

Issued by Sandia National Laboratories, operated for the United States Department of Energy by Sandia Corporation.

Available to DOE and DOE contractors from
U.S. Department of Energy
Office of Scientific and Technical Information
P.O. Box 62
Oak Ridge, TN 37831

Telephone: (865) 576-8401
Facsimile: (865) 576-5728
E-Mail: reports@adonis.osti.gov
Online ordering: http://www.osti.gov/bridge

Available to the public from
U.S. Department of Commerce
National Technical Information Service
5285 Port Royal Rd
Springfield, VA 22161

Telephone: (800) 553-6847
Facsimile: (703) 605-6900
E-Mail: orders@ntis.fedworld.gov
Online ordering: http://www.ntis.gov/help/ordermethods.asp?loc=7-4-0#online

SAND2015-20782
Unlimited Release
Printed January, 2015

An Attempt to Calibrate and Validate a Simple Ductile Failure Model Against Axial-Torsion Experiments on Al 6061-T651

Benjamin Reedlunn
Sandia National Laboratories
P.O. Box 5800
Albuquerque, NM 87185-0840

Wei-Yang Lu
Sandia National Laboratories
P.O. Box 969
Livermore, CA 94550-9042

Abstract

This report details a work in progress. We have attempted to calibrate and validate a Von Mises plasticity model with the Johnson-Cook failure criterion (Johnson & Cook, 1985) against a set of experiments on various specimens of Al 6061-T651. As will be shown, the effort was not successful, despite considerable attention to detail. When the model was compared against axial-torsion experiments on tubes, it over predicted failure by 3× in tension, and never predicted failure in torsion, even when the tube was twisted by 4× further than the experiment. While this result is unfortunate, it is not surprising. Ductile failure is not well understood. In future work, we will explore whether more sophisticated material models of plasticity and failure will improve the predictions. Selecting the appropriate advanced material model and interpreting the results of said model are not trivial exercises, so it is worthwhile to fully investigate the behavior of a simple plasticity model before moving on to an anisotropic yield surface or a similarly complicated model.

Acknowledgment

We would like to acknowledge Helina Jin for her help collecting and analyzing the digital image correlation data, and William Scherzinger for reviewing this manuscript. We also appreciate several helpful discussions with Edmundo Corona, Kevin Long, and Jacob Ostien.

Contents

List of Figures

Chapter 1

Introduction

Sandia analysts frequently wish to know when severe plastic deformations will cause a metal component to break. Predicting exactly when failure will occur can be a challenge because the scientific community has yet to agree on the proper approach to model ductile failure. Instead, analysts will often use ductile failure models to just compare one design to another, or they will ensure that important results of the analysis do not hinge on precisely predicting the time and location of a crack. These kinds of strategies are prudent and appropriately conservative, but it would clearly be better if we had failure models we could trust across a wide range of defamation modes.

Much of what makes ductile failure a difficult research area is local measurements of the failure strains are rare in the literature. To circumvent this, many researchers employ a hybrid approach that combines experiments and simulations to quantitatively estimate the failure strains (e.g. Wierzbicki *et al.* (2005); Faleskog & Barsoum (2013)). Typically, experiments on various geometries are performed in a load frame, while monitoring the far-field load and displacement. These measurements are then compared against simulations using the finite element method, or detailed analytical calculations with simplifying assumptions. If the comparisons are favorable, then the model's predictions of the local strain to failure for a given load path are used to calibrate a failure model. This means that accurate predictions of failure hinge on accurate predictions of all the plasticity up to the initiation of failure. Many plasticity models can produce reasonable predictions of gross plasticity, but the strain localization that often precedes failure is much more difficult to predict. Strain localization can be quite sensitive to the plasticity model, mesh densities, and geometric/material defects.

In some cases, the confidence in the strain field predictions is enhanced by comparing against measured strain fields. This approach is certainly an improvement over comparing against only far-field measurements, but macroscopic strain field measurement techniques, such as digital image correlation (Sutton *et al.* , 2009), frequently require a significant degree of smoothing to distinguish the signal from the noise. If a sharp strain localization occurs prior to failure, then a model is still required to predict the strain to failure. In a departure from most papers in the ductile failure literature, Ghahremaninezhad & Ravi-Chandar (2013) and Haltom *et al.* (2013) performed local, grain level, measurements of the strain to failure on Al-6061-T6. They found that it was difficult to precisely quantify the failure strain because the localization occurred on such a small scale, but both concluded that the equivalent

plastic strain to failure monotonically decreased with increasing triaxiality (mean stress over equivalent stress). Such scientific studies are worthwhile endeavors, however, grain measurements are not practical on an engineering scale. One cannot perform in-depth experiments and metallography on every combination of processing parameters used to manufacture a metal component. Until we have an efficient method to measure highly localized strains, it is still valuable to continue to develop the hybrid approach of combining experiments and simulations to calibrate ductile failure models.

Chapter 2

Modeling Approach

Here, we compare a simple Von Mises plasticity model with the Johnson-Cook failure criterion (Johnson & Cook, 1985) against a series of experiments on Al 6061-T651 bars and tubes. Smooth bar tension (Fig. 2.1(a)), compression, notched bar tension (Fig. 2.1(b)), smooth tubes (Fig. 2.1(c)), and notched tubes (Fig. 2.1(c)) specimens were all machined from the same large bar of Al-6061 shown in Fig. 2.1(a). Many of these experiments were previously published (Lu & Jin, 2014), but the compression data, failed specimen images, and several repeat experiments contained herein are new.

(a) Smooth bars

(b) Notched bars

(c) Smooth tube and notched tube

Figure 2.1. Photos of the specimens

The smooth bar tension and notched bar tension specimens were used to calibrate the plasticity and failure model, while compression experiments and tension-torsion experiments on the tube specimens were used to attempt to validate the model. We could have calibrated the failure model against the notched tube experiments, and validated against the notched bar experiments, but we wished to explore how a model calibrated against straightforward experiments can predict more elaborate experiments.

All finite element simulations were performed using Sierra/Solid Mechanics implicit quasi-statics v. 4.32 and v. 4.34 (Sierra/Solid Mechanics, 2014). Meshes were generated with

CUBIT (CUBIT, 2014). The element type was q1p0, which has a fully integrated ($2 \times 2 \times 2$ quadrature) deviatoric response, and a under integrated (1-point quadrature) pressure response.

No attempt was made to model crack propagation. Simply deleting elements once they meet the failure criterion can cause problems for implicit finite element solvers, and can also lead to mesh sensitive results. Fortunately, the initiation of cracks was always very distinct in the experiments studied here. Either crack propagation occurred in an unstable manner, such that crack initiation virtually coincided with ultimate failure, or there was a sudden drop in load and a macroscopic crack was observed in the specimen surface. This scenario allowed us to focus on crack initiation and leave propagation for future work.

Chapter 3

Model Calibration

Most constitutive models for ductile failure fall into two categories: uncoupled models and coupled models. Uncoupled models consist of a plasticity model with an independent failure criterion attached to it. Material failure occurs when the failure criterion reaches a critical value. In coupled models, the plastic response depends on the amount of damage (e.g. void growth) that occurs during plastic deformation. Material failure occurs when the damage reaches a critical value. Coupled models may be more physically realistic, but they are also harder to calibrate. We typically do not have direct experimental measurements of damage during mechanical deformation, so the extent of damage must be inferred by comparing other measurements against simulation results. Such inferences are possible with accurate measurements of damaged and damage free material behavior through the range of interest, but those measurements are not always available.

In this work, we elected to use an uncoupled ductile failure model. This choice allowed the plasticity model to be calibrated independent of the failure model, and it allowed an efficient failure model calibration scheme that will be discussed in Section 3. Convenience, however, was not the only motivation for this decision. Ghahremaninezhad & Ravi-Chandar (2012) cross-sectioned Al 6061-T6 notched tension specimens at various stages prior to failure and detected a void area fraction greater than 1% only when the specimen was within $\approx 1\%$ of the failure displacement. Furthermore, they cross-sectioned a failed specimen and found virtually no voids at distances of greater than 30 μm beneath the fracture surface. These results suggest that voids do not play a significant role in the plastic response of Al 6061-T6. Voids may be a bigger factor in more ductile materials, such as stainless steel, which can sustain the extreme local deformations needed to accommodate cavities without failing.

Elasticity Model

The elastic behavior of the aluminum was modeled using a simple isotropic, linear-elastic, material model. The value for Young's modulus $E = 68.9$ GPa and Poisson's ratio $\nu = 0.33$, were taken from the median values listed in Table 2 of Ledbetter (1982) for Al 6061-T6.

Plasticity Model

A simple J_2-flow model with isotropic hardening and a multilinear hardening curve was used to capture the aluminum plasticity. The model is rate and temperature independent, which suffices for Al-6061 tested at isothermal, quasi-static rates, in room temperature air (Hoge, 1966; Lindholm & Yeakley, 1968). In the Sierra/Solid Mechanics manual (Sierra/Solid Mechanics, 2014), this model is known as the Multilinear Elastic-Plastic Hardening Model, but it is important to note that we did not use the tearing parameter failure model that is typically paired with this plasticity model. (As discussed in Section 3, the failure model was Johnson-Cook.)

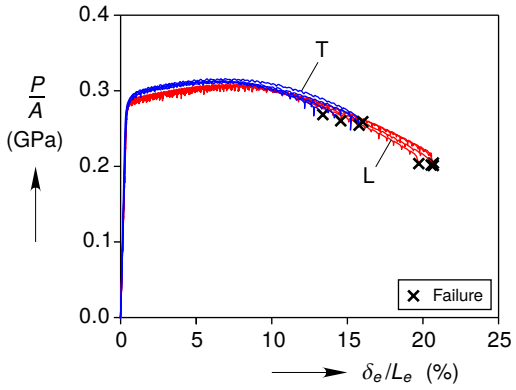

Figure 3.1. Experimentally measured smooth bar engineering stress–strain curves along the transverse (T) and longitudinal (L) directions. Four specimens were tested in each direction.

The tensile specimens used for calibrating the hardening curve are shown in Fig. 2.1(a) and Fig. 3.2(a), and the corresponding mechanical response curves are shown in Fig. 3.1. Four specimens were oriented in the longitudinal (L) direction and four were oriented in the transverse (T) direction. All eight specimens were round, dogbone, bars with a diameter $2R$=2.54 mm and a distance between the fillets L of approximately 16.5 mm (see Fig. 3.2(a)). The vertical axis in Fig. 3.1 is the axial force P over the original cross-sectional area A, and the horizontal axis is the mechanical extensometer displacement δ_e over the extensometer gage length L_e = 7.62 mm. The specimens did not have a defect to ensure necking would occur in the same location, so some of the variation in the mechanical response curves after the maximum load could be due to the neck forming at various locations within the extensometer gage length. The transverse specimens have an approximately 10 MPa higher yield stress than the longitudinal specimens, which persists until the maximum load. During necking, the transverse specimens have a slightly more negative tangent modulus and fail at a roughly 25% smaller value of δ_e/L_e than the longitudinal specimens. It should be noted, however, that the central gage section of the transverse specimens came from the center of the large bar in Fig. 2.1(a), while the central gage section of the longitudinal specimens

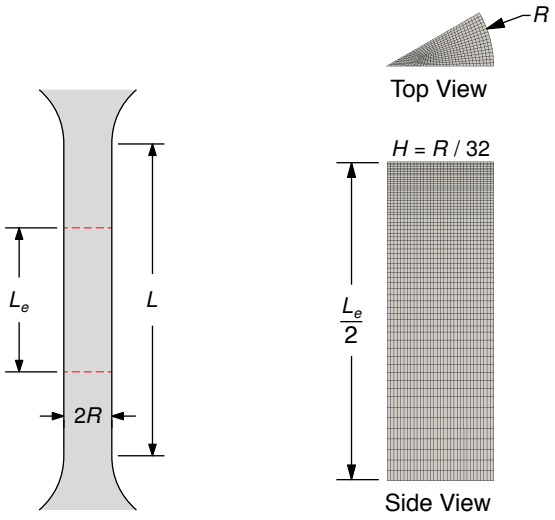

(a) Specimen schematic

(b) FE Mesh

Figure 3.2. Smooth bar geometry and finite element discretization.

came from regions near the circumference of the large bar. Thus, there appears to be a small amount of anisotropy in the plastic response, and a large amount of anisotropy in the failure displacement, but it is possible some of the anisotropy is actually spatial variation of properties in the large bar.

The mesh used to simulate the tension tests is shown in 3.2(b). The deformation was assumed to be symmetric about the mid-plane, so only the bottom half of the extensometer gage length was modeled. The loading and the specimen are axisymmetric, but Sierra/SM (Sierra/Solid Mechanics, 2014), does not include axisymmetric elements. Fortunately, a 30° wedge with the appropriate boundary conditions is an accurate substitute. The decision to model only the extensometer gage length, the angle of the wedge, the element size of $H = R/32$, and the simulation time step size are all justified in Appendix A.1. In order to trigger the necking localization at the center of the bar length, the mesh was tapered with a radius of R at the symmetry plane, and a radius of $1.0005R$ at the bottom extensometer knife edge.

The piecewise linear hardening curved was obtained by an inverse method programmed into a Python script. Starting from the user specified yield stress, the inverse method found the slopes of 50 to 70 linear hardening segments. For a given linear hardening segment, a hardening slope was guessed and the mechanical force–displacement response from the finite element simulation was compared with the experimental response. If the agreement was unacceptable, slope was iterated on until acceptable agreement was reached. If the agreement was acceptable, the slope was stored and the calibration routine moved to the next linear hardening segment. This trial-and-error process continued until the entire mechanical

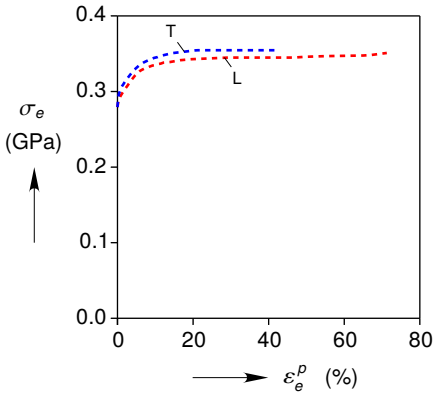

(a) Calibrated hardening curves

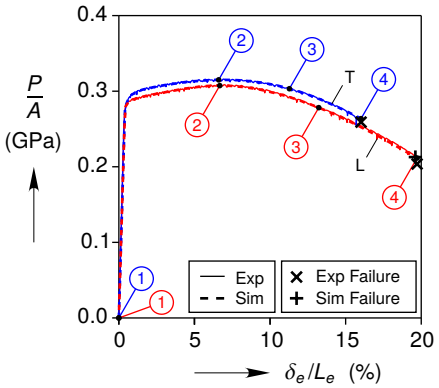

(b) Mechanical responses

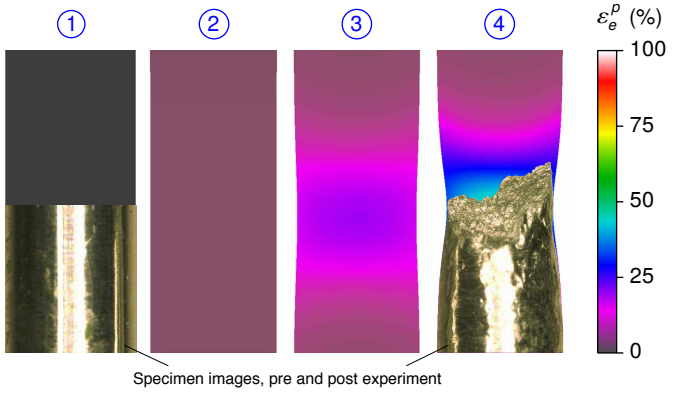

(c) Transverse deformed shapes

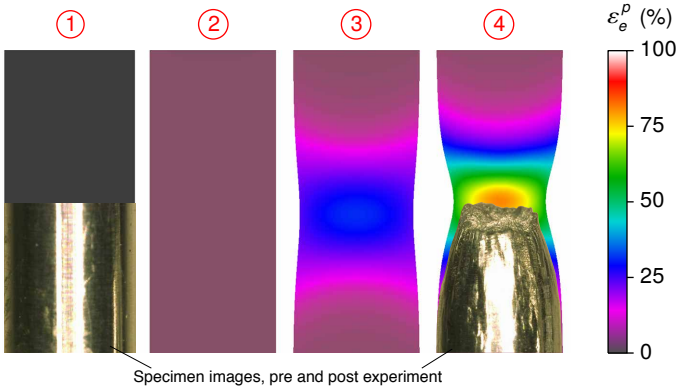

(d) Longitudinal deformed shapes

Figure 3.3. Two separate hardening curve calibrations to one tensile experiment along the transverse (T) direction and one experiment along the longitudinal (L) direction. The predicted deformed shape (overlaid with contours of equivalent plastic strain) is also compared against specimen images before and after tensile tests, for the transverse and longitudinal specimens. The circled numbers above the images in (c) and (d) correspond to the instances in (b).

response of the specimen was recovered in the simulation.

Two hardening curve calibrations were obtained: one against a longitudinal specimen and one against a transverse specimen. The hardening curves and mechanical response curves are shown in Fig. 3.3(a) and (b). The variables σ_e and ε_e^p are the Von Mises equivalent stress and Von Mises equivalent plastic strain. The predicted and measured mechanical responses agree very well, and the hardening curves have shapes that are typical of a Von Mises plasticity model calibrated against Al 6061. (See Fig. 13b in Tardif & Kyriakides (2012) for a comparison of hardening curves for different yield surfaces calibrated against the same tensile response curve.) As expected, the transverse hardening curve is about 10 MPa higher than the longitudinal. Perhaps more interesting is the fact that the transverse curve terminates at $\varepsilon_e^p = 41.9$ %, while the longitudinal terminates at $\varepsilon_e^p = 71.3$ %. Clearly, the difference in the failure displacements in (b) gets amplified in the equivalent plastic strain to failure.

Piecewise linear hardening can represent the tensile plastic behavior of nearly any material, so it is instructive to also compare the predicted shape of the neck against the experiment to evaluate other assumptions in the model. Figure 3.3(c) and (d) depict the deformed shape predictions overlaid with contours of equivalent plastic strain. The figures also include images of the specimens taken before the experiment and after tensile failure. (Strictly speaking, the failed specimens should be compared against simulations that have been unloaded to zero load, but the elastic part of the deformation is small compared to the plastic.) The transverse model calibration does quite a good job of predicting the deformed shape of the transverse specimen. The longitudinal calibration does not have enough lateral contraction to accurately predict the deformed shape, but the discrepancy is not excessive.

Presuming for a moment that the large aluminum bar is transversely isotropic, then the transverse specimen should have necked anisotropically. A more in depth comparison between the isotropic model and the experimental measurements would include an image perpendicular to both the longitudinal and transverse directions. The longitudinal specimen, on the other hand, should have an axisymmetric neck, so no further comparisons are needed.

To further examine the plasticity model predictions, Fig. 3.4 compares compression simulations from the two hardening curve calibrations against compression experiments in the transverse and longitudinal directions. Provided the compression platens are made frictionless, compression specimens deform in a homogenous manner to far larger strain magnitudes than tension specimens that suffer from the tensile necking instability. Homogeneous uniaxial compressive stress means the compression specimen (see Fig. 3.4(a)) with diameter $2R$=5.08 mm and length L=8.89 mm can be modeled with a single element (see Fig. 3.4(b)). Of course, it is nearly impossible to have zero friction at the compression platens, but Kawahara (1990) developed a method to minimize it. The compressive responses are shown in Fig. 3.4(c) with the tensile responses for reference. The horizontal axis δ/L is the engineering strain across the compression platens. The displacement at the platens δ was calculated from the the actuator stroke measurement, with a small correction factor to compensate for the axial compliance of the load stack (see Kawahara (1990) for details). Note that the elastic modulus in the compression experiments should be disregarded because the initial stiffness

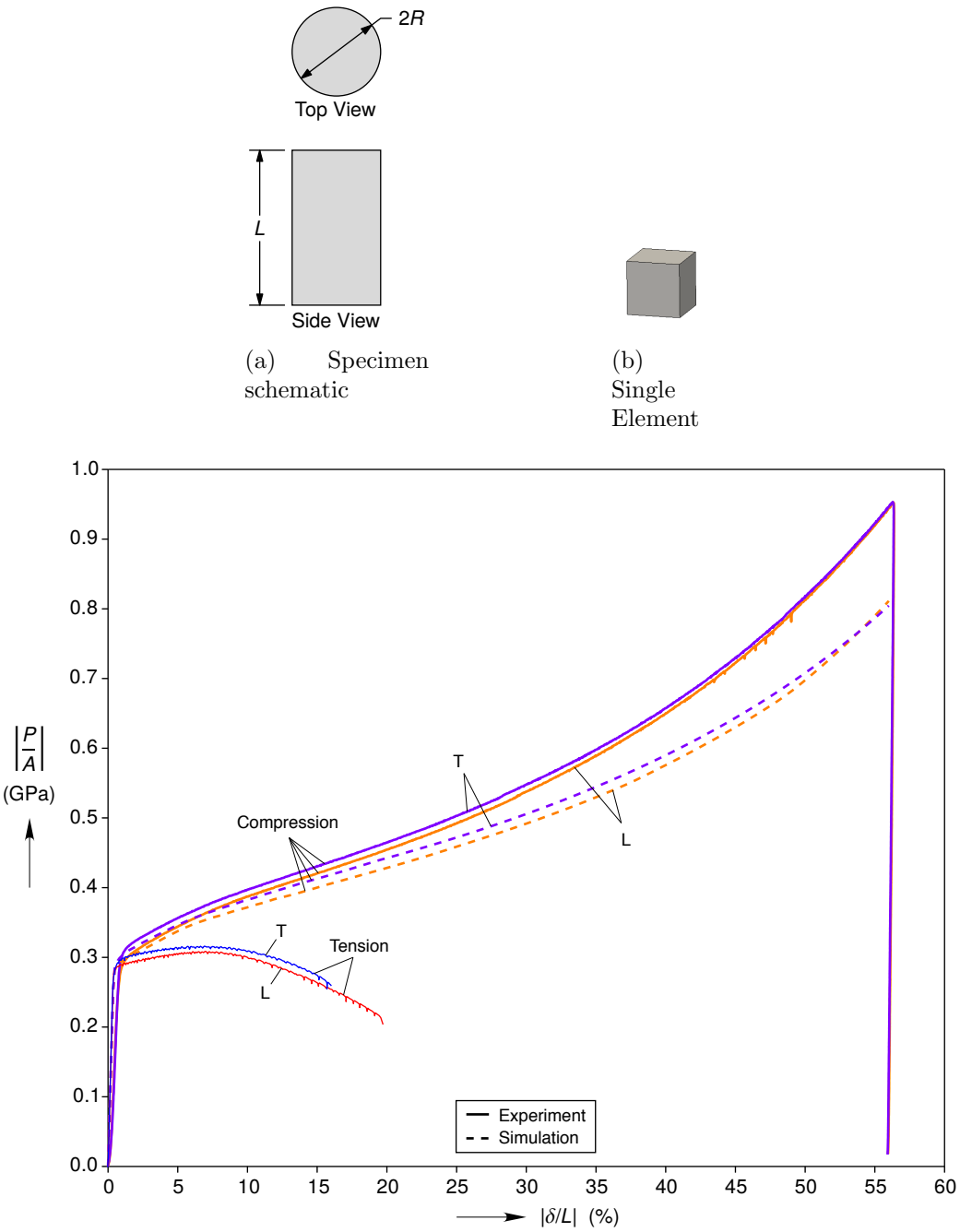

(a) Specimen schematic

(b) Single Element

(c) Mechanical responses

Figure 3.4. Compression specimen geometry, finite element mesh, and mechanical responses along the transverse (T) and longitudinal (L) directions. The compression simulations used the T and L hardening curves shown in Fig. 3.3a. The measured tension stress-strain curves are included for reference.

is affected by the platens engaging the specimen. Keeping in mind that the specimens did slightly "barrel" during the experiments, the simulations match up reasonably well with the experiments up to $|\delta/L| \approx 25\%$. The discrepancy beyond $|\delta/L| \approx 25\%$ may be due to increased barreling, or it may be due to inadequacies in the model. Further investigation would be needed to track down the cause.

Thus far we have shown results from the transverse and longitudinal hardening calibrations in tandem, but from here onward we will only consider the longitudinal calibration. The notched tension bars, notched tubes, and smooth tubes (Fig. 2.1(b) and (c)) were all machined from the large Al-6061 bar with the same orientations as the longitudinal tensile specimen in Fig. 2.1(a), so it is only natural to proceed with the longitudinal hardening curve calibration.

Failure Model

We elected to use the phenomenological Johnson-Cook failure model (Johnson & Cook, 1985) due to its simplicity and because the recent results by Haltom *et al.* (2013) indicate that failure of Al-6061-T6 exhibits a exponential dependence on the stress triaxiality. For isothermal, rate-independent, failure, the Johnson-Cook model reduces to three model parameters d_1, d_2, and d_3, which relate the stress triaxiality η to the equivalent plastic strain to failure ε^p_{ef} through the following equation

$$\varepsilon^p_{ef} = d_1 + d_2 \exp\left[d_3\,\eta\right]. \tag{3.1}$$

If η is constant, then (3.1) is sufficient, but η is not constant through the deformation history in nearly all practical experiments. In the more general case, the integral

$$D = \int_0^{\varepsilon^p_e} \frac{\mathrm{d}\hat{\varepsilon}^p_e}{\varepsilon^p_{ef}}, \tag{3.2}$$

sums each $\mathrm{d}\varepsilon^p_e$ increment, normalized by the equivalent plastic strain to failure ε^p_{ef} for the current value of η, to calculate D. If $D \geq 1$, then failure occurs.

The failure model parameters d_i were calibrated against the the longitudinal smooth bar tension results previously discussed and results from three different notched bar geometries (shown in Fig. 3.5(a)). The three notched bar geometries provide a wide range of stress triaxialities when pulled, and they are frequently found in the ductile failure literature (e.g. Wierzbicki *et al.* (2005); Faleskog & Barsoum (2013)). First, we will discuss the predictions of the notch bar plastic responses, and, second, we will discuss the failure model calibration.

The notched bar geometry, finite element meshes and mechanical responses are shown in Fig. 3.5. In all three notched bar specimens, the radius $R = 6.35$ mm and the mechanical extensometer gage length $L_e = 25.4$ mm (Fig. 3.5(a)). The notched bar geometries were discretized into the meshes shown in Fig. 3.5(b). The decision to model only the extensometer gage length, the angle of the wedge, and the element size of $H = R/24$ are all justified in

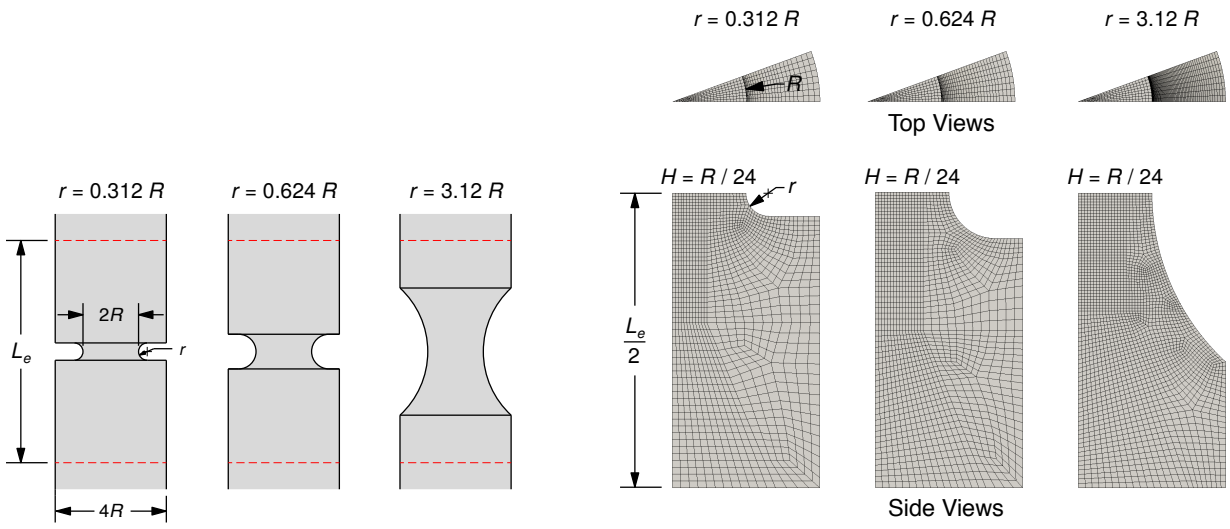

(a) Schematics

(b) FE meshes

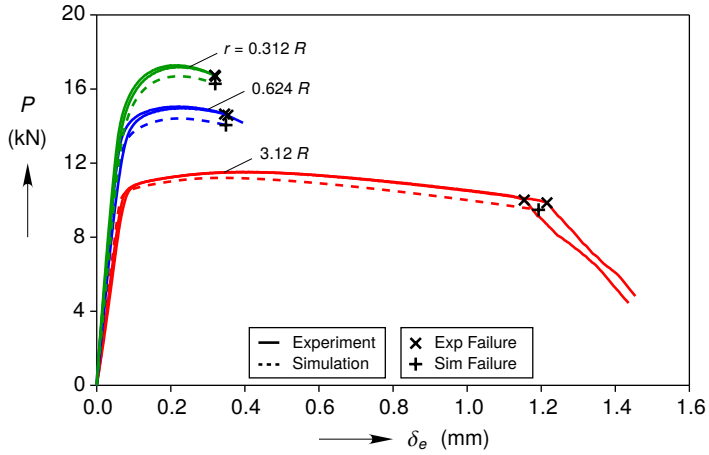

(c) Mechanical responses

Figure 3.5. Notched bar specimen geometry, finite element meshes, and mechanical responses. The mechanical response plot contains two experiments and one simulation for each geometry.

Appendix A.2. Two experimental curves are compared against one simulation of each notch geometry in the plot of axial force P versus extensometer displacement δ_e (Fig. 3.5(c)). The mechanical response predictions are reasonably accurate in all three cases. The $r = 3.12\,R$ prediction is probably the most accurate because the deformation is closest of the three to the smooth bar tension calibration of the hardening curve.

An efficient failure model calibration scheme was developed to quickly iterate on the model parameters d_i. Although the process of calibrating a path dependent, uncoupled,

d_1	d_2	d_3
0.034	5.73	-3.17

(a) Model parameters

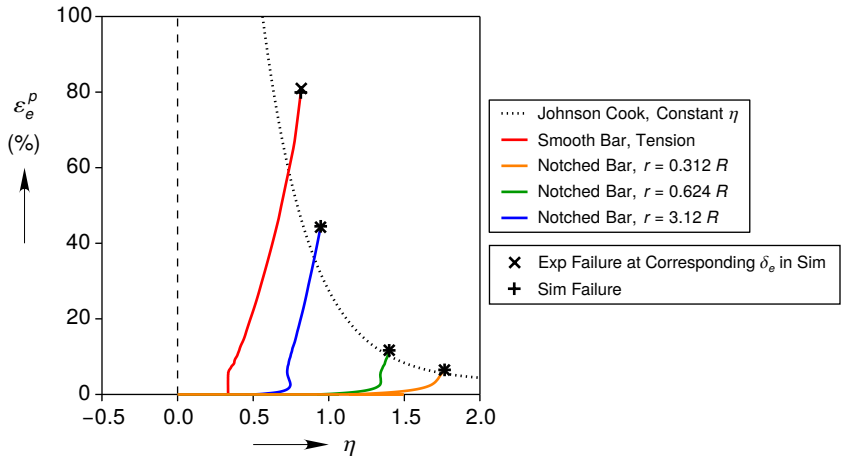

(b) Evaluation of the calibration

Figure 3.6. Calibration of the Johnson Cook failure model. (a) contains the calibrated model parameters, while (b) depicts the ε_e^p versus η path for the first point to fail in each of the calibration simulations. See text for further description.

failure model is easier than a failure model coupled to a plasticity model, it still requires requires many iterations of the same finite element simulation. Each time you change the failure model parameters, it is possible a different material point, with a different stress-strain history, will fail first. Here, however, it was clear that failure would occur in a small region, so we simply output the Cauchy stress $\boldsymbol{\sigma}$ and the equivalent plastic strain ε_e^p at every time step for the elements in the failure region. Then, $\boldsymbol{\sigma}$ and ε_e^p were imported into Python and D was calculated for a given set of d_i. In this manner, simulations could be run well past failure once and the d_i could be changed without rerunning the simulations, which greatly sped up the calibration optimization process.

The three model parameters d_i were optimized against four experiments, using the L-BFGS-B algorithm (Zhu *et al.* , 1997). The resulting failure model parameters are listed in Fig. 3.6(a). One can evaluate the quality of the fit by examining the longitudinal curve in Fig. 3.3(b) and the three notched bar curves in Fig. 3.5(c). Figure 3.6(b) is another depiction of the calibration results, where the first point to fail in the simulation is plotted in ε_e^p–η space. Each curve also has a + symbol to indicate when the first point failed in the simulation, and a $\times$ symbol to indicate when the average of the two specimens failed in the experiments. Obviously, we did not measure ε_e^p or η in the experiment, so the $\times$ symbol coordinates come from correlating the failure displacement δ_e in the experiment to

the simulation displacement δ_e, and then selecting the corresponding values of ε_e^p and η from the simulation. Fig. 3.6(b) also includes a plot of equation (3.1) as a dashed line to help guide the reader's eye, and show when the model predicts failure for a state of constant η. The value of η primarily increases in all the simulations, so it is not surprising that the failure predictions are beyond the dashed line. In summary, the model calibration is satisfactory.

Chapter 4

Validation Effort

The model was compared against a series of tension-torsion experiments on notched tubes and smooth tubes. The notched tube validation effort is more extensive, so the discussion below focuses on the notched tubes, but the smooth tube comparison can be found in Appendix B.

The notched tube specimen geometry is shown in Fig. 4.1(a), along with the coordinate systems used to report some of the results. The tube actually has two notches, one on the outer diameter, one on the inner diameter, resulting in a wall thickness $B = 0.508 \pm 0.025$ mm at the apex of the notch. The inner diameter notch was machined with a specialized, hook-shaped, tool on a computer numerically controlled (CNC) machine. The length of the specimen between the grips, was approximately 50 mm. The axial displacement and angle of twist was measured using stereo digital image correlation (DIC)(Sutton *et al.* , 2009) on the outside surface of the tube. A virtual extensometer measured the axial displacement δ_e and the transverse displacement δ_x between two points separated by $L_e = 16$ mm. One point was 8 mm above the notch apex and the other was 8 mm below the notch apex. Both points were on the line where the $X = 0$ plane intersects the undeformed tube outer surface. (See Fig. 10a in Lu & Jin (2014) for plots of the transverse displacement along this line.) The angle of twist between the two points was calculated as $\phi_e = \arcsin(\delta_x/C)$, where C is the tube radius in the thick wall region (see Fig. 4.1(a)).

Three different meshes (see Fig. 4.1(b)) were used for the three different loading conditions, but the three meshes shared two common features. (1) Mid-plane symmetry was assumed for all three meshes, so it was only necessary to model the bottom half of the specimen. (2) The deformation was assumed to be spatially uniform in the vicinity of the virtual extensometer knife edges, so it was not necessary to model the specimen material outside the extensometer gage length. The tension specimen was modeled using a thin 2° wedge to take advantage of the axisymmetric nature of the problem, but the combined tension-torsion and the torsion problem required a full 360° mesh to simulate the twisting motion. Mesh convergence studies were performed on all three boundary value problems, resulting in 108, 36, and 18 elements across the notch thickness in the tension, combined tension-torsion, and torsion specimens, respectively. The details of the mesh convergence study can be found in Appendix A.3.

The notched tube simulations are compared against the experiments in Fig. 4.2, where the mechanical response predictions are reasonable, but the failure predictions are quite

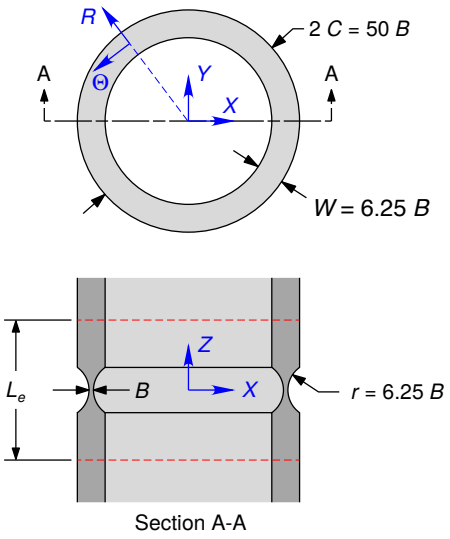

(a) Specimen schematic

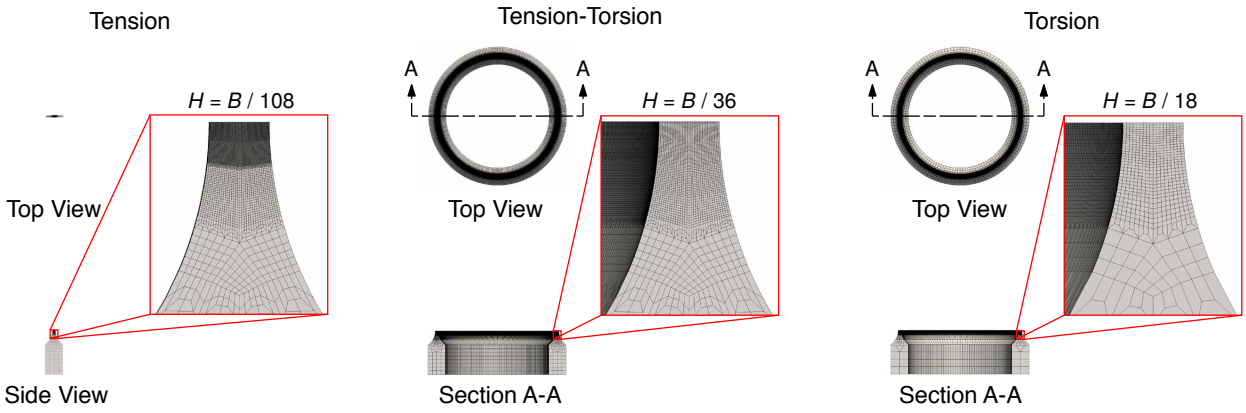

(b) FE meshes

Figure 4.1. Notched tube specimen geometry and finite element meshes.

poor. Two experiments and one simulation were performed for each loading condition. Figure 4.2(c) shows the deformation paths, where it is evident that δ_e and ϕ_e were controlled to follow linear paths in the tension and tension-torsion simulations. A preliminary study (see Appendix A.3) found that following the precise deformation path measured in the experiment did not significantly change the failure predictions, so the linear paths were used for simplicity. In the torsion simulation, ϕ_e was prescribed and the axial force P was held to zero to mimic the conditions in the experiment. Interestingly, the torsion simulation predicts a slight elongation, which is consistent with the Poynting effect (Poynting, 1909), but an axial contraction is observed in the experiment. Perhaps the mechanical response measurements in Fig. 4.2(d) and (e) are the most revealing. In tension, the experiments reach the maximum load and fail, while the simulation slightly over predicts the post yield

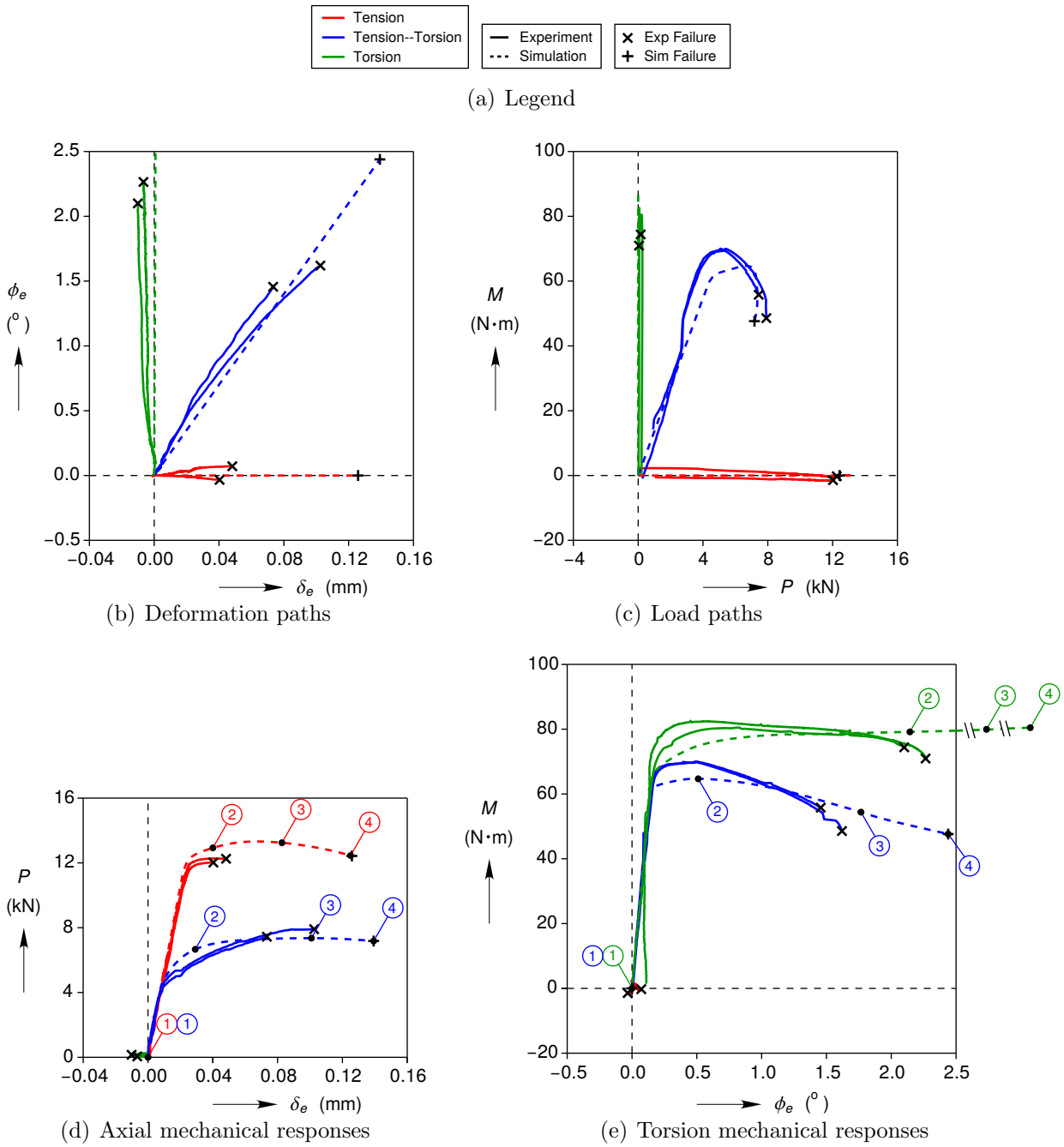

(a) Legend

(b) Deformation paths

(c) Load paths

(d) Axial mechanical responses

(e) Torsion mechanical responses

Figure 4.2. Notched tube experiments compared against simulations. The plots contain two experiments and one simulation for each general loading type. The torsion simulation does not predict failure, despite having twisted the tube four times beyond the experiments (circled labels 3 and 4 on the torsion curve in (e) are at $\phi_e = 5.5^o$ and 9.0^o, respectively). The circled labels correspond to the field images in Fig. 4.4.

load and over predicts the failure displacement by roughly 3×. In combined tension-torsion,

the experiments and the simulation exhibit a local maximum in the torque M without a corresponding maximum in the load. The prediction of the failure displacement is better in the tension-torsion simulation than in the tension simulation, but it is still about 50% too large. In pure torsion, the experiments have an intriguing local maximum in the torque long before ultimate failure. A decreasing force–displacement curve in tension can indicate a necking instability, but necking instabilities typically do not occur in torsion, so this is a curious result. As expected, the simulation predicts a monotonically increasing torque. The torsion experiments fail at $\phi_e \approx 2.2°$, while the simulation never predicted failure, despite having twisted the mesh to $\phi_e = 8.8°$. In all cases, the predictions of the axial load and torque leave a little to be desired, but the predictions of failure are lamentable. The remainder of this report will explore why.

The reason the torsion simulation never failed becomes clear when we consider Fig. 4.3, but the poor predictions in the other two simulations are more difficult to understand. Similar to Fig. 3.6(b), the ε_e^p–η paths for the first points to fail in the notched tube simulations are plotted in Fig. 4.3, along with the average failure points in the experiments, at the corresponding value of δ_e in the simulation. The four failure model calibration points are shown for reference. The triaxiality in pure torsion remains roughly 0 throughout the simulation. If we input $\eta = 0$ into (3.1), then failure is not predicted until $\varepsilon_{ef}^p = 576$ %, which is long way from the $\varepsilon_e^p = 72$ % reached when the simulation was at the failure twist angle measured in the experiment. While not encouraging, the poor prediction in torsion is not terribly surprising since the model was calibrated at high triaxialities. The poor predictions in combined tension-torsion and, especially, tension are more troubling. The notched tube tension-torsion simulation is close to the same triaxiality as the smooth bar tension calibration point, and the notched tube tension simulation is even between the two of the failure model calibration points.

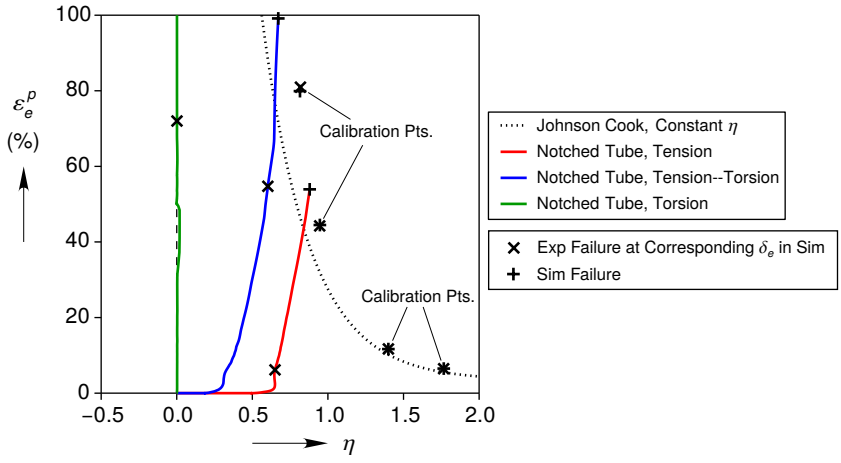

Figure 4.3. Notched tube failure predictions compared against experiments. The failure model calibration points are shown for reference.

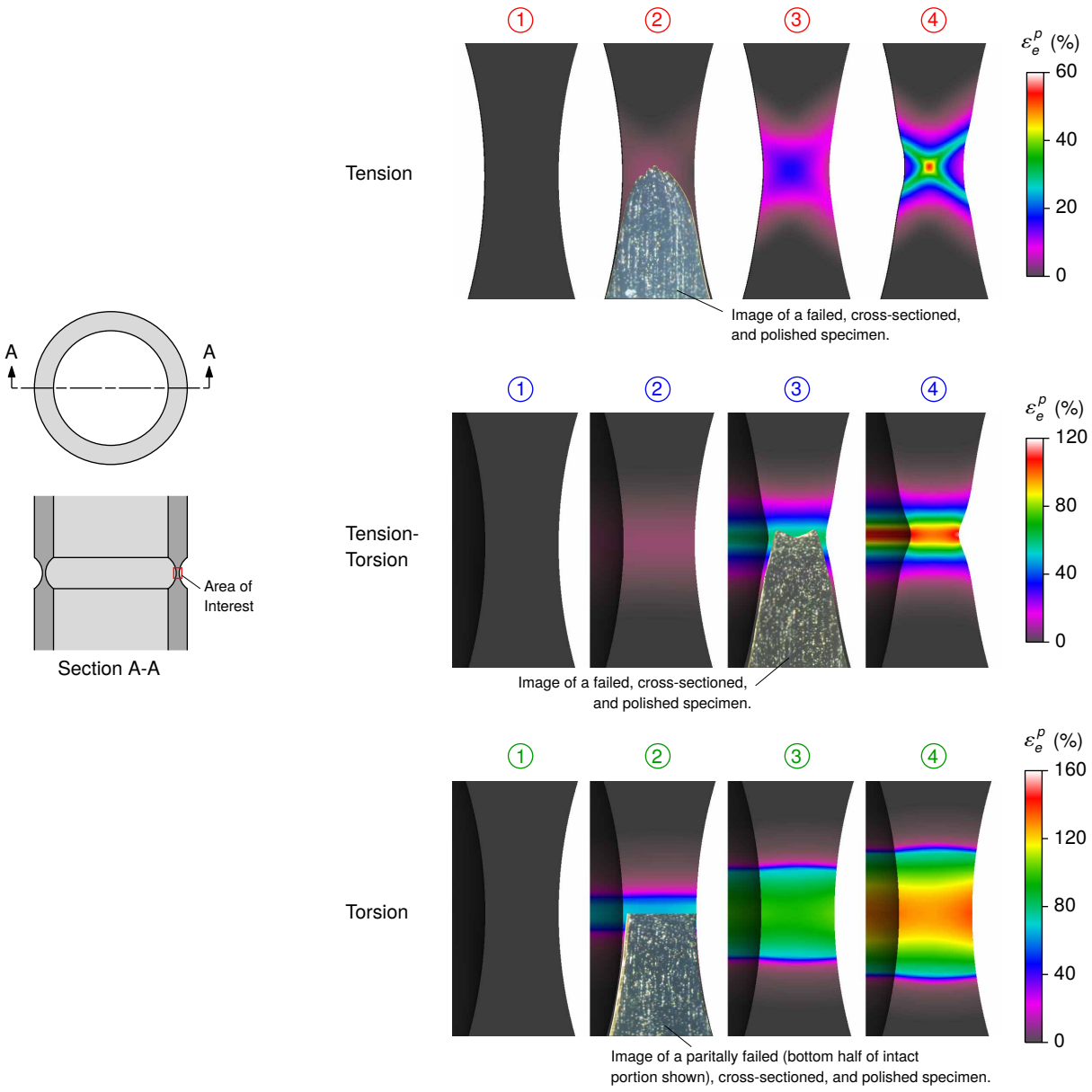

Figure 4.4. Predictions of the deformed thin wall section of the notched tube, compared against images from the experiments. The circled letters and numbers above the field images correspond to the instances in Fig. 4.2(d) and (e).

The plasticity model and the failure model were calibrated against a smooth bar tension experiment, so one would expect the model to produce a decent prediction of the tensile failure in the double notched tube. On the other hand, the shoulders above and below the notch are 6.25 times thicker than the thin wall at the notch apex, so they constrain the ability of the notch to contract in the hoop direction as the tube is pulled along the Z-direction.

This constraint causes a significant hoop stress, which changes the lode angle at the failure point. We briefly considered switching from the Johnson-Cook failure criterion to a lode angle dependent failure criterion, but it is not prudent to fiddle with the failure model until one is certain that the plasticity model is accurately predicting the deformation.

A comparison between the predictions of the deformed shape against cross-sections of failed specimens sheds some light on the cause for the poor failure prediction in the tension and tension-torsion simulations. The circled number instances in Fig. 4.2(d) and (e) correspond to the deformed shapes with overlaid contours of equivalent plastic strain in Fig. 4.4. Instance ② in tension, ③ in tension-torsion, and ② in torsion were carefully chosen to correspond with the values of δ_e and ϕ_e when one of the two specimens tested in each configuration failed in the experiments. Those failed specimens were cross-sectioned and polished in order to capture the images shown overlapping the bottom half of the deformed shape predictions in ②, ③, and ②. The tension simulation predicts minimal deformation, while the specimen clearly developed a significant neck through the wall thickness in the experiment. The tension-torsion simulation does predict through thickness necking in ③, but the amount is under predicted. Finally, the torsion shape prediction agrees with the experimentally observed shape, but that is simply because the shear specimen did not appreciably deform in the thickness direction.

The deformed shape comparisons show that the plasticity model does not capture the strain localization prior to failure. Until this shortcoming is rectified, we cannot evaluate the applicability of the failure model. Localization is known to be very sensitive to boundary conditions, imperfections, and material properties, so two attempts were made to see if small changes could induce necking in the notched tube tension simulation.

Machining the notch on the inner diameter of the tube is a relatively involved operation, and it is possible that the notch wall thickness was not entirely uniform. This possibility was investigated by shifting the inner notch cutout axis of revolution to one side, resulting in a wall thickness $B + e$ on one side and $B - e$ on the other side (see Fig. 4.5(b)). An eccentric inner notch destroys the axisymmetry of the boundary value problem, and leads to a small amount of bending as the specimen is pulled, so the tension mesh in Fig. 4.1(b) was not used. Instead, 180° of the specimen was modeled, taking advantage of the $X - Z$ plane symmetry, and the entire 50 mm between the grips was meshed. Note that the number of elements across the notch was reduced from 108 to 18 to make these simulations more tractable. The mechanical responses and failure predictions for two different eccentricities are compared against a nominal notched tube simulation with 18 elements across the notch in Fig. 4.5(c). An eccentricity of $e = 0.05B$ corresponds to the tolerance on the notch wall thickness (± 0.025 mm), yet the defect makes very little difference on when the strain localizes and the failure criterion is met.

Al-6061-T651 is quite prone to tensile strain localization due to its mild hardening after initial yield. The point where the hardening curve becomes flat often leads to localization because the equivalent plastic strain can increase without an increase in the equivalent stress, so Fig. 4.6 explores the impact of artificially making the hardening curve go flat at $\varepsilon_e^p = 20$ % and $\varepsilon_e^p = 10$ %. Shifting the flat point from $\varepsilon_e^p = 30$ % (the original calibration) to $\varepsilon_e^p = 20$ %

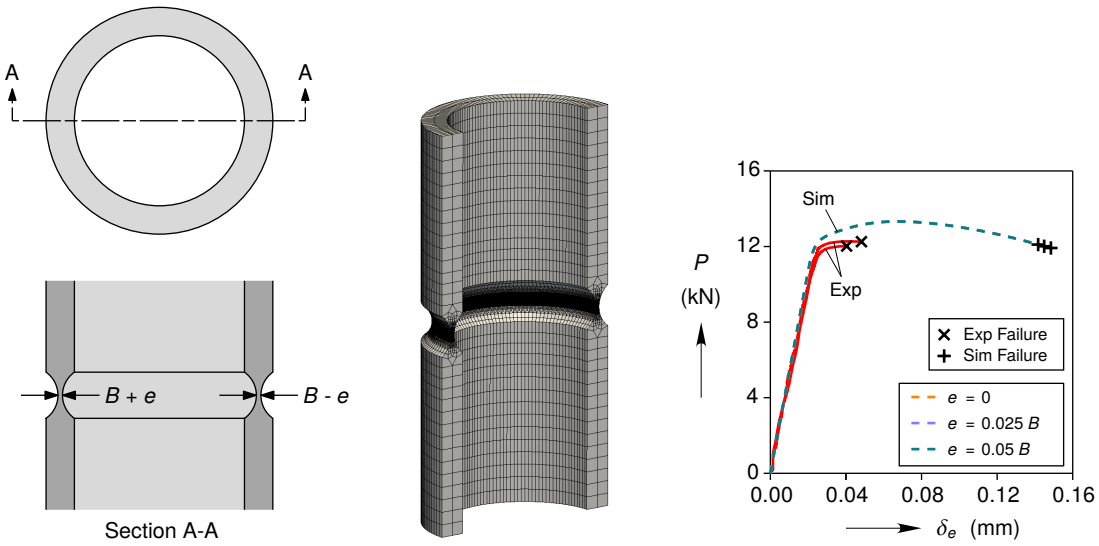

(a) Schematic (b) FE mesh (c) Mechanical response

Figure 4.5. Defect sensitivity of the notched tube tension predictions. The defect was created by shifting the center of the notch on the inner diameter laterally, away from the centerline of the tube.

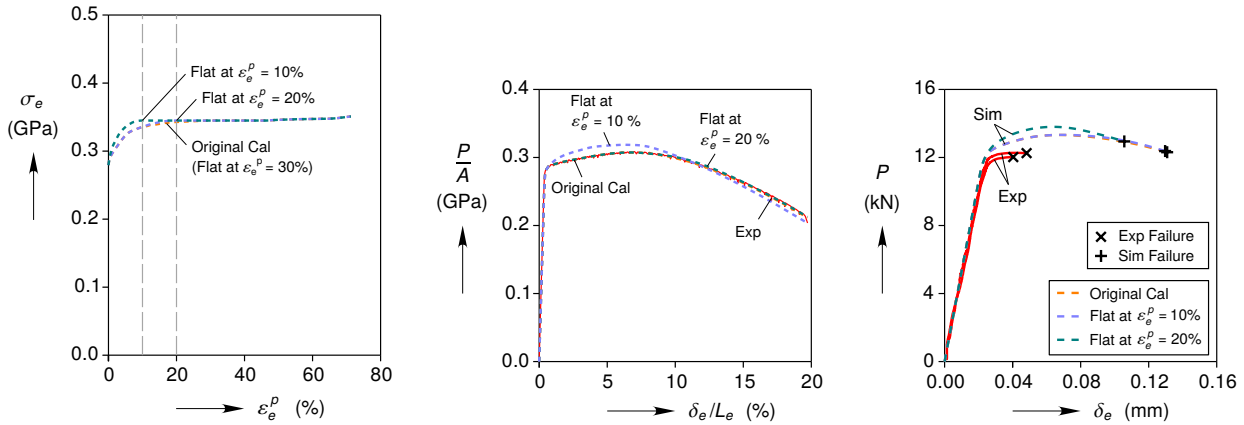

(a) Hardening curves (b) Smooth bar tension responses (c) Notched tube tension responses

Figure 4.6. Hardening curve sensitivity of the smooth bar tension and notched tube tension predictions.

preserves the smooth bar tension response (Fig. 4.6(b)), but it also produces a negligible change in the notched tube tension simulation (Fig. 4.6(c)). A more extreme shift of the flat point to $\varepsilon_e^p = 10$ % violates the smooth bar tension calibration and appreciably changes the notched tube tension simulation, but the strain still localizes, triggering failure, far beyond the experiment. The necking instability in this problem does not appear to be highly sensitive to the hardening curve shape.

Chapter 5

Discussion

In an effort to understand why the plasticity model does not accurately capture the strain localization in tension or tension-torsion, the principal Cauchy stress paths for the first points to fail were plotted in the π-plane (Fig. 5.1(a)). We have ordered the three principal stresses such that $\sigma_1 < \sigma_2 < \sigma_3$. The π-plane is a bit difficult to look at because none of the three principal stress axes actually lie in the π-plane, so we will start with some explanations. First, the calibration stress paths appear to be all along the σ_3 axis, but they also have a mean stress component, which is perpendicular to the π-plane. Second, pure shear is simply a combination of tension and compression in the principle frame, so $\sigma_1 < 0$ and $\sigma_3 > 0$ for the notched tube torsion stress path, causing it to be 30° to the right of the σ_3 axis projected onto the π-plane. Third, observe that the tension and tension-torsion stress paths exhibit a sharp change in direction when they hit the initial yield surface. To unravel why the stress paths change direction, we consider the plots of stress against simulation time $\bar{t}$ in Fig. 5.1(b) and (c).

Let us look at the notched tube tension stress path first. The failure point in the tension simulation does not experience shear, so the stress histories in the global cylindrical frame (top plot in Fig. 5.1(b)) are the same as the stress histories in the principle frame (bottom plot in Fig. 5.1(b)). In the linear-elastic range, the simulation predicts axial stress and a significant hoop stress because the large shoulders constrain the lateral Poisson contraction of the notch in the hoop direction. This is why the stress path follows a radial line to the right of the σ_3 projection in the π-plane. When the notch begins to plastically deform, the hoop constraint plays a bigger role because the plastic strains are isochoric. This causes the hoop strain to sharply increase and the stress path to sharply turn to the right in the π-plane after initial yield.

The notched tube tension-torsion stress path follows a similar progression, but the shear stress $\sigma_{\Theta Z}$ makes the explanation more complicated. Pure shear is simply a combination of tension and compression in the principle frame. Here, $\sigma_{\Theta Z}$ serves to increase the largest principle stress σ_3 and decrease the smallest principle stress σ_1, while leaving the intermediate principle stress σ_2 untouched. In the linear-elastic range, the hoop constraint again causes hoop stress along with the axial stress, but the shear stress makes σ_1 become negative in Fig. 5.1(c). This is why the tension-torsion stress path also follows a radial line to the right of the σ_3 projection in the π-plane. Between $\bar{t} = 0.08$ and $\bar{t} = 0.23$, yielding begins, the shear stress remains relatively constant, and the hoop stress quickly increases, which causes

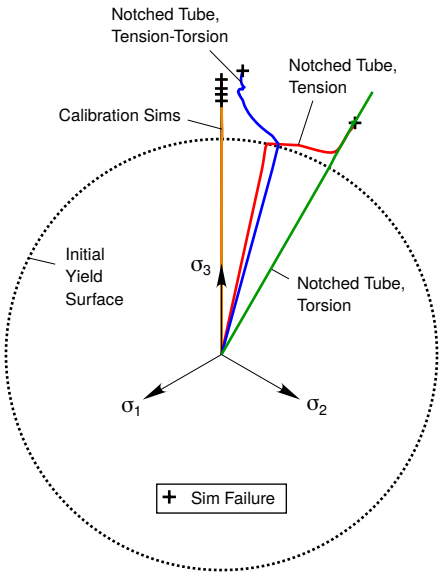

(a) π-plane

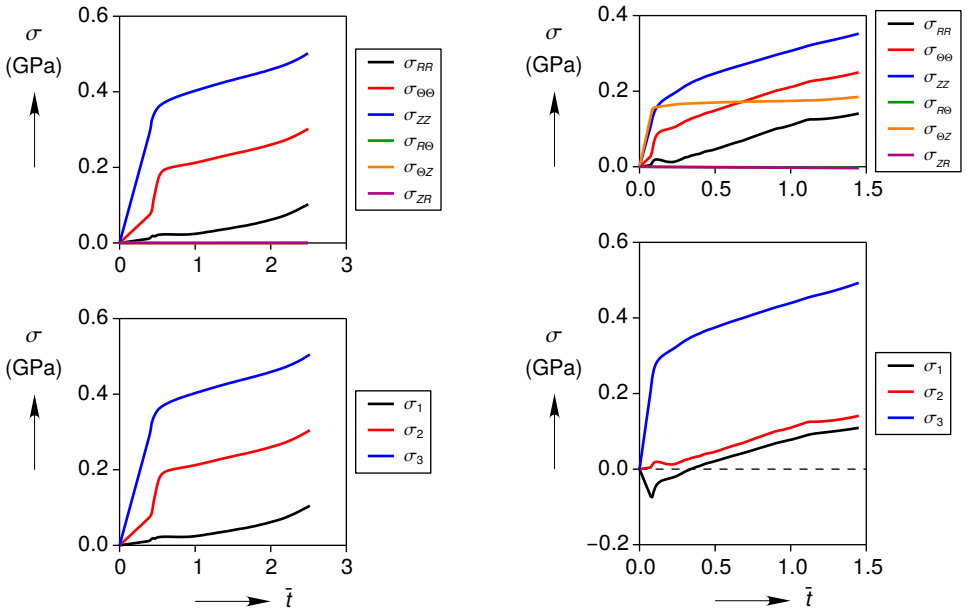

(b) Tension stress histories

(c) Tension-torsion stress histories

Figure 5.1. (a) Cauchy stress paths in the π plane for the first point to fail (or come closest to failing) in the calibration simulations and notched tube simulations. (b) and (c) Cauchy stress histories for the notched tube in tension, and the notched tube in tension-torsion. The top plots in (b) and (c) are the stress component histories in the global cylindrical coordinate system, while the bottom plots are the principle stress histories.

σ_1 to increase by 52 MPa, while σ_2 only increased by 9 Mpa. This is why the stress path turns to the left, towards the projection of the σ_3 axis in the π-plane.

Now that we have established why the stress paths are those shown in Fig. 5.1(a), we can make some observations which suggest a non-quadratic or anisotropic yield surface could improve the plasticity predictions and, by extension, improve the failure predictions. We note again that the stress paths in Fig. 5.1(a) are for the first point to fail in each simulation. Not all material points in a given specimen follow the stress paths in Fig. 5.1(a), but the spread is likely small enough that qualitative comparisons between the stress paths can be made in order to decide how to proceed from here.

- The predictions of the mechanical response in the notched bar and notched tube simulations all start to deviate from the experiments at the onset of plasticity, yet the notched tube deviations are worse than the notched bar. This is likely because the axial core of the notched bar follows stress paths in Fig. 5.1(a) that closely align with the smooth bar tension stress path that was used to calibrate the plasticity model. The notched tube stress paths, on the other hand, all probe portions of the yield surface to the right of where the hardening curve was calibrated.
- The notched tube torsion mechanical response prediction deviates the most from the experiment (Fig. 4.2(e)), and, of all the stress paths, the notched tube torsion stress path is the furthest from the smooth bar tension calibration in the π-plane.
- The notched tube tension simulation and tension-torsion simulation both had trouble predicting the deformed shape of the notch. The same two simulations also produce stress paths that penetrate the initial yield surface and then quickly turn to almost trace along the yield surface as it isotropically grows.
- The notched tube tension-torsion simulation did a better job of predicting the deformed notch shape and the eventual failure than the notched tube tension simulation. This could be related to the observation that the tension-torsion stress path turns towards smooth bar tension stress path, while the tension stress path turns away from where the isotropic hardening curve was calibrated.

The notched tube plastic response appears to be sensitive to the shape of the yield surface, but it remains to be seen if the yield surface actually deviates enough from Von-Mises to make a significant difference in the notched bar and notched tube predictions. The transverse smooth bar measurements in Fig. 3.1 only have a 3.5 % larger yield stress than the longitudinal, so it seems hard to believe that could significantly change things. On the other hand, strain localizations are quite sensitive to anisotropy. Ghahremaninezhad & Ravi-Chandar (2012) measured less than 2 % difference in yield stresses between the rolling, 45°, and transverse directions on thin sheet specimens, yet they predicted a 17 % lower force at failure with the anisotropic model compared to the isotropic model. Perhaps more importantly, the local strain values predicted by the anisotropic model were in better agreement with the experimental measurements with maximum values that were 2× those in the isotropic model.

For the next material model, we plan to start with a specialization of the Hill (1948) model to transverse isotropy, matched up with the Johnson Cook failure criterion. One could also consider using a Gurson-type model which causes the yield surface shape to evolve as damage accumulates, but damage does not start to accumulate in such models until well after yield. The J_2-theory model used here started to deviate from the experiments at the onset of yield, so it is better to alter the initial yield surface. Furthermore, as previously mentioned, there is no evidence of damage until immediately prior to failure in Al-6061 (Ghahremaninezhad & Ravi-Chandar, 2012). It is possible Johnson Cook failure model will still be inadequate to capture the experimental measurements, but we will be in a much better position to prove that if we accurately capture the plasticity.

Chapter 6

Conclusions

A simple Von Mises plasticity model and the Johnson Cook ductile failure model were calibrated and compared against experiments on Al-6061. Although the plasticity model predictions of the global force and torque measurements were decent, the predictions of ductile failure in a notched tube were quite poor. The model over predicted the notched tube failure by 300 % in tension, over predicted by 50 % in tension-torsion, and never predicted failure in torsion, even when the tube was twisted 400 % further than the experiment. The model was calibrated against tension and notched tension experiments, so the poor predictions of failure in the notched tube tension and tension-torsion experiments were particularly troubling.

Careful comparisons with cross sectioned, failed, notched tube specimens revealed that the plasticity model did not accurately predict a necking instability prior to failure. One cannot evaluate a ductile failure model unless one can properly predict the plasticity up to failure, so efforts were made to induce the necking instability. A mesh refinement study, a defect sensitivity study, and a hardening curve sensitivity study all did not have the desired effect.

Further analysis led to the belief that an anisotropic yield surface is needed to capture the plasticity behavior. Anisotropic plasticity models are more involved to calibrate and their results can be difficult to interpret, so the experience gained from the isotropic Von Mises plasticity model used herein should aid in future work.

References

CUBIT. 2014. *CUBIT users manual*. 14.0 edn. Sandia National Labs, P.O. Box 5800, Albuquerque, NM, USA.

Faleskog, Jonas, & Barsoum, Imad. 2013. Tension–torsion fracture experiments—Part I: Experiments and a procedure to evaluate the equivalent plastic strain. *International Journal of Solids and Structures*, **50**(25), 4241–4257.

Ghahremaninezhad, A, & Ravi-Chandar, K. 2012. Ductile failure behavior of polycrystalline Al 6061-T6. *International journal of fracture*, **172**(2), 177–202.

Ghahremaninezhad, A, & Ravi-Chandar, K. 2013. Ductile failure behavior of polycrystalline Al 6061-T6 under shear dominate loading. *International journal of fracture*, **180**(1), 23–39.

Haltom, SS, Kyriakides, S, & Ravi-Chandar, K. 2013. Ductile failure under combined shear and tension. *International Journal of Solids and Structures*, **50**(10), 1507–1522.

Hill, Rodney. 1948. A theory of the yielding and plastic flow of anisotropic metals. *Proceedings of the Royal Society of London. Series A. Mathematical and Physical Sciences*, **193**(1033), 281–297.

Hoge, Kenneth G. 1966. Influence of strain rate on mechanical properties of 6061-T6 aluminum under uniaxial and biaxial states of stress. *Experimental Mechanics*, **6**(4), 204–211.

Johnson, Gordon R, & Cook, William H. 1985. Fracture characteristics of three metals subjected to various strains, strain rates, temperatures and pressures. *Engineering fracture mechanics*, **21**(1), 31–48.

Kawahara, WA. 1990. EFFECTS OF SPECIMEN DESIGN IN LARGE-STRAIN COMPRESSION. *Experimental Techniques*, **14**(2), 58–60.

Ledbetter, H.M. 1982. *Physical Properties Data Compilations Relevant to Energy Storage. V. Mechanical Properties Data on Alloys for Use in Flywheels*. National Bureau of Standards.

Lindholm, US, & Yeakley, LM. 1968. High strain-rate testing: tension and compression. *Experimental Mechanics*, **8**(1), 1–9.

Lu, Wei-Yang, & Jin, Helena. 2014 (July). An experimental study of ductile failure under multi-axial loading. *Page V06AT06A011 of: Proceedings of the ASME 2014 Pressure Vessels & Piping Division Conference*. American Society of Mechanical Engineers.

Poynting, JH. 1909. On pressure perpendicular to the shear planes in finite pure shears, and on the lengthening of loaded wires when twisted. *Proceedings of the Royal Society of London. Series A, Containing Papers of a Mathematical and Physical Character*, **82**(557), 546–559.

Sierra/Solid Mechanics. 2014. *Sierra/solid mechanics user's guide.* 4.34 edn. Sandia National Labs, P.O. Box 5800, Albuquerque, NM, USA.

Sutton, Michael A, Orteu, Jean-José, & Schreier, Hubert W. 2009. Image correlation for shape, motion and deformation measurements. *Springer, New York*.

Tardif, Nicolas, & Kyriakides, Stelios. 2012. Determination of anisotropy and material hardening for aluminum sheet metal. *International Journal of Solids and Structures*, **49**(25), 3496–3506.

Wierzbicki, T., Bao, Y., Lee, Y.W., & Bai, Y. 2005. Calibration and evaluation of seven fracture models. *International Journal of Mechanical Sciences*, **47**(4), 719–743.

Zhu, Ciyou, Byrd, Richard H, Lu, Peihuang, & Nocedal, Jorge. 1997. Algorithm 778: L-BFGS-B: Fortran subroutines for large-scale bound-constrained optimization. *ACM Transactions on Mathematical Software (TOMS)*, **23**(4), 550–560.

Appendix A

Preliminary Studies

A number of preliminary studies were performed before settling on the final analyses shown in the main body of the report. This section of the appendix records those studies.

A.1 Smooth Bar

Ductile failure predictions depend heavily on the quality of the plasticity model calibration, so it is worthwhile to perform the calibration carefully. We first made our best guess at the proper approach and modeling parameters to simulate the smooth bar tension test, and generated the longitudinal hardening curve shown in Fig. 3.3(a). Then those guesses were tested by comparing against other approaches and parameters.

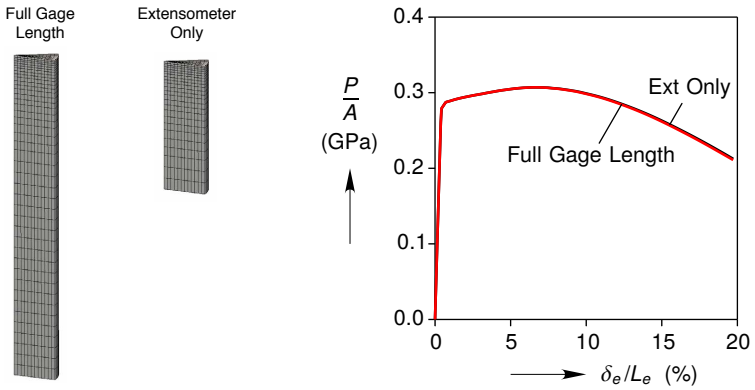

(a) Meshes (b) Mechanical response

Figure A.1. A comparison between modeling the entire smooth bar gage length against modeling only the extensometer gage length (assuming symmetry about the mid plane).

Figure A.1 depicts the difference between modeling the entire gage length between the grips against only modeling the extensometer gage length, and it makes negligible difference.

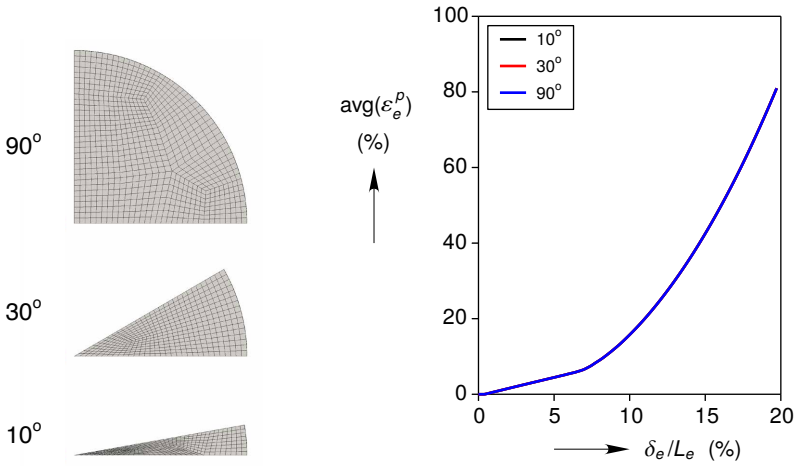

(a) Meshes (b) Equivalent plastic strain

Figure A.2. A comparison between modeling the smooth bar specimen as a 10°, 30°, and 90° wedge. The equivalent plastic strain (ε_e^p) was averaged over the element at the center of the tensile specimen, as denoted by the avg(·) operator.

The neck that develops after the maximum load makes the deformation non-uniform. If the region of appreciable necking extends beyond the extensometer knife edges, then a simulation that forces the material to deform uniformly at the extensometer knife will over-constrain the boundary value problem. In this case, the necking region is sufficiently far from the knife edges that modeling only the extensometer gage length is acceptable.

The effect of three different wedge angles are considered in Fig. A.2, and the angle made no difference. Poorly shaped elements are known to produce inaccurate results in certain scenarios, and the element at the tip of the 10° wedge specimen in Fig. A.2(b) might be considered suspect. To investigate this we examined the equivalent plastic strain, the lode angle, and the triaxiality at the wedge tip element, where the neck occurs. The wedge angle had no effect on all of these local variables important to failure modeling, as well as the mechanical response prediction, which is dominated by elements far from the wedge tip. Only ε_e^p is shown to conserve space. The highest value of ε_e^p was not always at the integration point closest to the wedge tip, varying in the 10th decimal place or higher, so we simply took an average of all nine q1p0 integration points to generate each data point in Fig. A.2(b). It is posited that the deformation, even inside the neck, is close enough to a principal deformation that the q1p0 element performs well at the wedge tip. Other elements may or may not perform similarly.

The mesh convergence on the mechanical response and the failure model prediction is shown in Fig. A.3, where each curve is labeled by the size of the elements along the bar radius R. At each mesh refinement, each element was split into eight elements. See Fig. 3.2(b) for an image of the mesh with 32 elements along the radius. The simulation with 16 elements

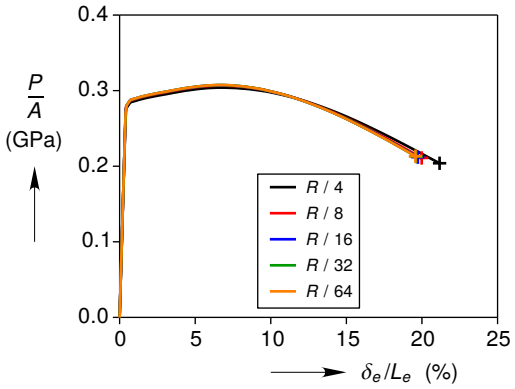

Figure A.3. Mesh convergence of the smooth bar mechanical response and failure.

along the radius is practically the same as the fine simulation with 64 elements along the radius (a 0.8 % difference at failure), but we elected to use 32 elements along the radius to be conservative.

The small sensitivity to the simulation time step $\Delta\bar{t}$ is displayed in Fig. A.4. Plasticity models are typically formulated in an incremental form that must be numerically integrated, so significant errors will be incurred if the time step is too large. Usually time step convergence studies are not performed in a practical setting because it is difficult to make the finite element solver converge if the time step is too large, and it is not terribly computationally expensive to take small time steps. Here, a quick time step convergence study was performed on the smooth bar tension simulation. Instead of fixing the time step for each simulation, which often results in simulations where the solver fails to converge, adaptive time stepping (Sierra/Solid Mechanics, 2014) with a maximum time step was utilized. This approach yielded the time step histories in Fig. A.4(a), where each history is labeled according to its maximum time step, and the total simulation time is $\bar{t} = 1$. All the time step histories first ramp up to their respective maximum values. When the specimen develops a neck, the time step sizes for $\max(\Delta\bar{t}_0)$ and $\max(\Delta\bar{t}_0)/2$ briefly dip to smaller values so that the solver can converge, while the other time step histories maintain their respective values. The time step's impact on the mechanical response curve and the failure prediction is minimal (Fig. A.4(b)), but we decided to use the smallest time step $\max(\Delta\bar{t}_0)/16 = 0.004$.

Strictly speaking, a time step convergence study should be performed on each boundary value problem, but the effort required was deemed excessive. Given the small sensitivity in Fig. A.4(b), we simply used adaptive time stepping on all simulations with a maximum time step of $\Delta\bar{t} = 0.004$, where $\bar{t} = 1$ is when failure was detected in the experiment.

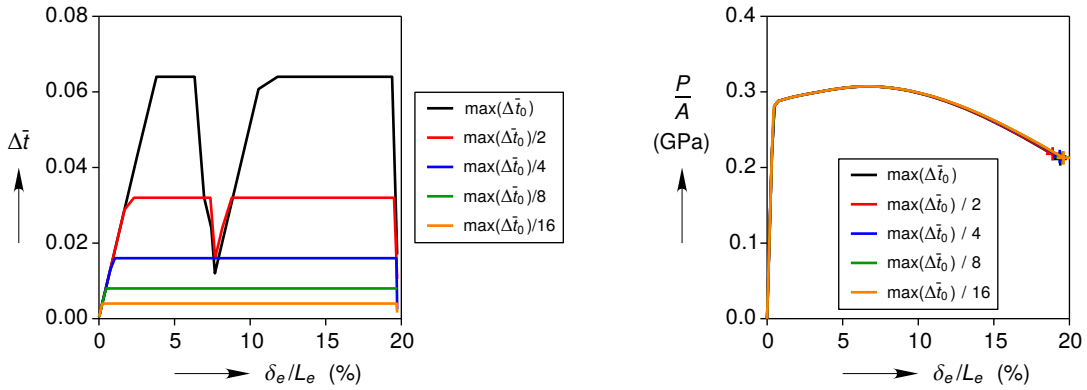

(a) Time step history

(b) Mechanical response

Figure A.4. Time step convergence of the smooth bar mechanical response and failure.

A.2 Notched Bar

The mesh convergence of the three notched bar geometries is shown in Fig. A.5, where each mesh is labeled according to the element size along the notch root radius R. At each mesh refinement, each element was split into eight elements. See Fig. 3.5(a) for images of the meshes with 24 elements across R. Not surprisingly, the mechanical response of tightest notch ($r = 0.16R$) is somewhat sensitive to mesh density. The failure prediction of the shallowest notch ($r = 1.56R$) is also a little bit sensitive to mesh refinement because the specimen develops a neck similar to the smooth bar tension simulation. In all three cases, the simulation with 24 elements across the notch root radius R was selected as sufficiently converged.

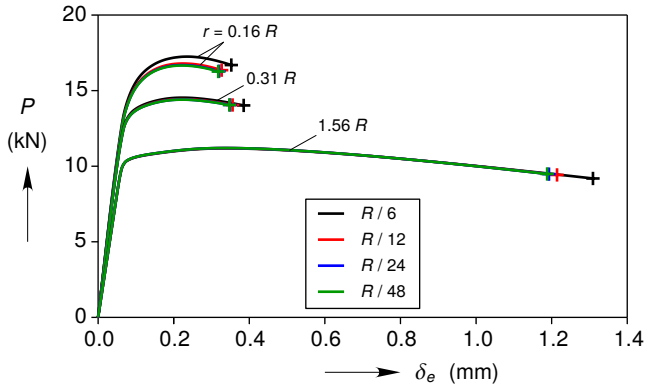

Figure A.5. Mesh convergence of the notched bar mechanical response and failure.

A.3 Notched Tube

Early in the effort to validate the material model against the notched tube experiments, a displacement path sensitivity study was performed. Although the notched tube tension and tension-torsion experiments were programmed to follow linear displacement paths, such a prescription is very difficult to achieve in reality. The load stack always stretches a small amount, the grips always slip, and the stress state near the grips is always complex. We simply measure the local displacement and rotation on the surface of the specimen and accept the non-linearity. In a simulation, however, we can compare the response for a linear displacement path (long dashes in Fig. A.6) to the response for the displacement path measured in the experiment (short dashes in Fig. A.6).

The sensitivity to the prescribed displacement path in ϕ_e–δ_e space is investigated in Fig. A.6. The simulations following the measured displacement path continue beyond the failure points in each experiment by linearly extrapolating the displacement path slope at failure. Considering the tension simulation first, the measured tension path in Fig. A.6(b) has a small amount of twist, which causes the simulation that follows the measured tension path to predict a torque reaching as high as $M = 19$ N·m. The torque prediction, however, does not correlate well with the experiment in Fig. A.6(c), where the measured torque does not exceed 2.5 N·m. Moving to the tension-torsion simulation, the mechanical response prediction does appear to be better when the simulation follows the measured displacement path. Exact magnitudes of P and M are not predicted in Fig. A.6(d) and (e), but the overall character of the prediction and the experiment are more consistent.

For simplicity, we decided to simply use linear displacement paths for all further simulations. It is strange that the torque predictions differ so much from the experiment in the tension simulation. The torque is quite sensitive to the angle of twist when the material is in the elastic range. Perhaps the twist measurement ϕ_e is accurate enough for plasticity

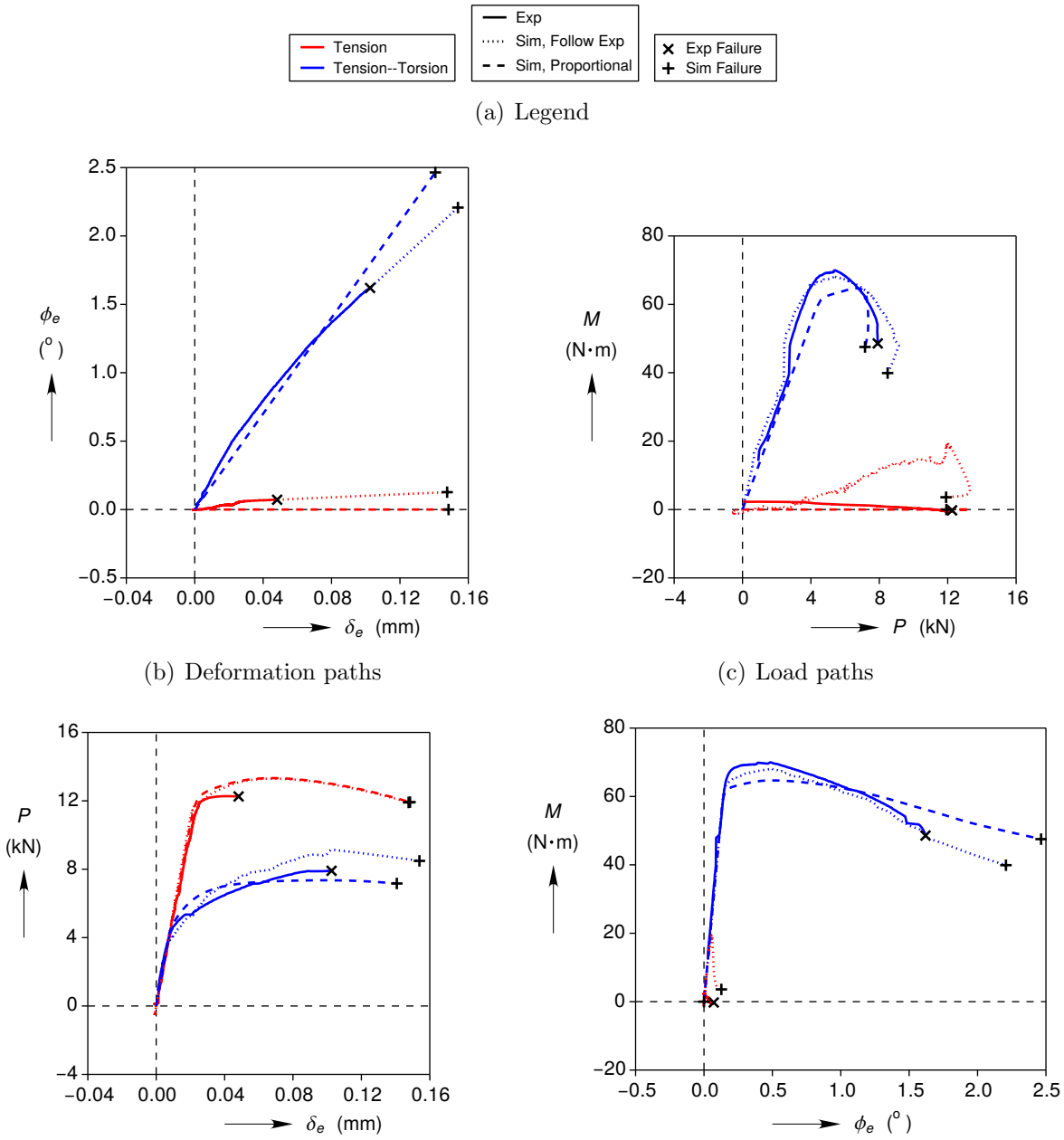

(a) Legend

(b) Deformation paths

(c) Load paths

(d) Axial mechanical responses

(e) Torsion mechanical responses

Figure A.6. Notched tube experiments compared against simulations that follow the experimentally measured displacement paths and those that follow proportional displacement paths.

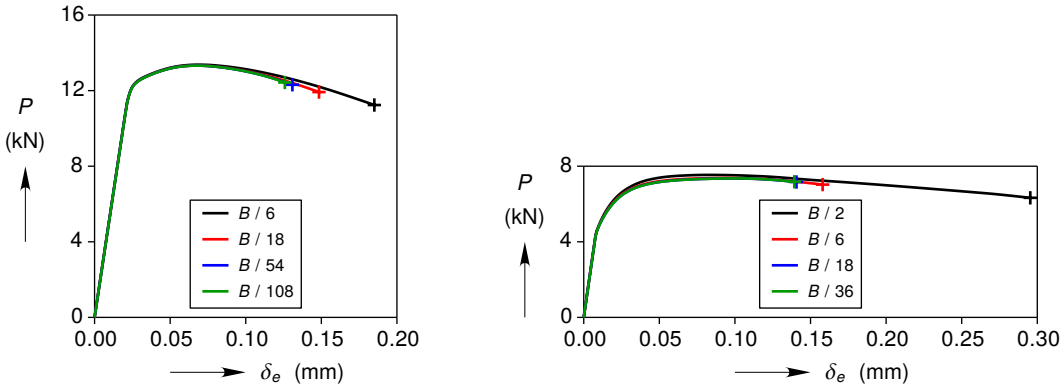

(a) Tension

(b) Tension-torsion

Figure A.7. Mesh convergence of the notched tube mechanical response and failure under two different deformations.

measurements, but not for elasticity measurements. Regardless, the prediction of failure did not improve when the measured path was followed in both tension and tension-torsion cases, so the linear displacement paths were deemed sufficient.

The simulations in Fig. A.6 all used 18 elements across the apex of the notch as a starting point, but mesh sensitivity studies were subseqently performed (see Fig. A.7). The first two mesh refinements involved locally splitting each element near the notch into 27 elements, along with a small transition region to the unrefined portion of the mesh. The third refinement was performed uniformly, where every element was split into eight elements. The meshes with 108 elements and 36 element across B are shown in Fig. 4.1(b). Although the tension simulation mechanical response appears converged with 18 elements through the notch, the failure displacement prediction still changes by 4 % as the mesh is refined from 54 to 108 elements. It is highly likely that another refinement would result in a minimal reduction in the failure displacement, so 108 elements was considered adequate. Clearly, a large number of elements is required to resolve the hot spot at the center of the "X" in the equivalent plastic strain field for ④ in Fig. 4.4. Fortunately, the tension-torsion boundary value problem only required 36 elements across B to converge.

The mesh convergence of the torsion simulation is shown separately in Fig. A.8, because it received a different treatment. Similar to the tension-torsion mesh convergence study, the first two mesh refinements on the torsion mesh were local refinements. A global refinement was planned, but the simulation with 18 elements across B took 48 hours on 32 processors. Increasing the element count by eight-fold would have been too computationally expensive, so we simply accepted the 18 elements across the notch. The mechanical response is clearly converged with 18 elements, but failure was never predicted in the model. Local mesh convergence was assessed instead using D, the Johnson-Cook failure indicator, and it is unlikely that a finer mesh would be significantly different than $B/18$ in Fig. A.3.

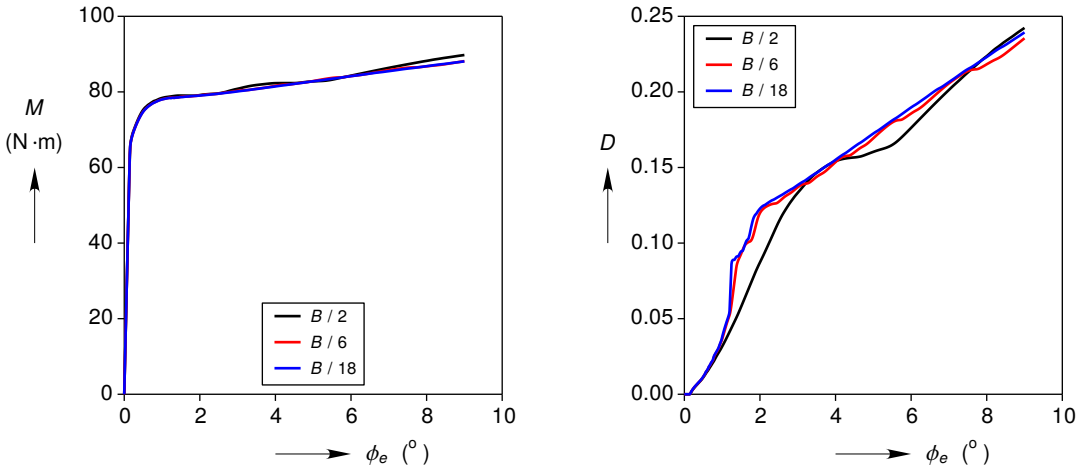

(a) Mechanical response

(b) Damage parameter

Figure A.8. Mesh convergence of the notched tube under torsion. None of the simulations predicted failure, so the Johnson-Cook failure indicator D for the point closest to failure at the end of each simulation is shown instead.

In an effort to find out why the torsion simulation was so slow, we found that the finite element solver struggled to converge when the material points at the notch apex reached the flat part of the longitudinal hardening curve in Fig. 3.3(a). The solver was probably having difficulty determining whether to assign a large amount of strain to the notch apex, or to assign a small amount of strain to the apex and the surrounding region.

Appendix B

Smooth Tube

The smooth tube geometry shown in Fig. B.1(a) has advantages and disadvantages compared to the notched tube.

- Machining the smooth tube to maintain the wall thickness $B = 0.508 \pm 0.025$ mm is likely easier than controlling the notched tube wall thickness at the notch apex.
- The smooth tube tends to buckle under pure torsion.
- The smooth section L_s=12.7 mm produces a more uniform strain field, so it is possible to make accurate measurements of the strain field using DIC, at least until the strain localizes immediately prior to failure.

We elected to focus the modeling effort on the notched tube instead of the smooth tube because of the inability to measure pure torsion failure in the smooth tube, but it may still be instructive to examine the smooth tube model predictions.

The smooth tube meshes are shown in Fig. B.1(b). Initially, the tension specimens were fully meshed with no symmetry assumptions to investigate if the strain localization prior to failure would break symmetry. A single node on the outer diameter was shifted inward by $0.0005B$ to create a defect, and three elements were used through the thin wall thickness for these simulations. Once we established that axisymmetry prevailed during the tension simulation, a 2° wedge was meshed with 54 elements through the thickness. The tension-torsion experiment was only simulated until shortly after yield, so only 2 elements were needed across B. In both smooth tube experiments, DIC measured the strain fields on the surface of the tube. We elected to use the Biot strain, which is defined as $\boldsymbol{E}^B = \boldsymbol{U} - \boldsymbol{I}$, where $\boldsymbol{U}$ is the right stretch tensor from the polar decomposition of the deformation gradient, and $\boldsymbol{I}$ is the identity tensor. The Biot strain fields were averaged over a surface area, roughly 9mm wide and 10mm tall, centered on the smooth thin wall section of the tube. In the simulations, we set the extensometer gage length to L_e=10 mm.

As shown in Fig. B.3(a) and (b), a sawtooth pattern of high strain was observed just prior to failure in the experiment, and sawtooth crack was observed afterwards. The primary author is also aware of unpublished tensile experiments on thin walled aluminum tubes that failed in a similar sawtooth fashion. These observations led to a study to see if the simulations could predict such patterns. Figure B.2 shows the experimentally measured

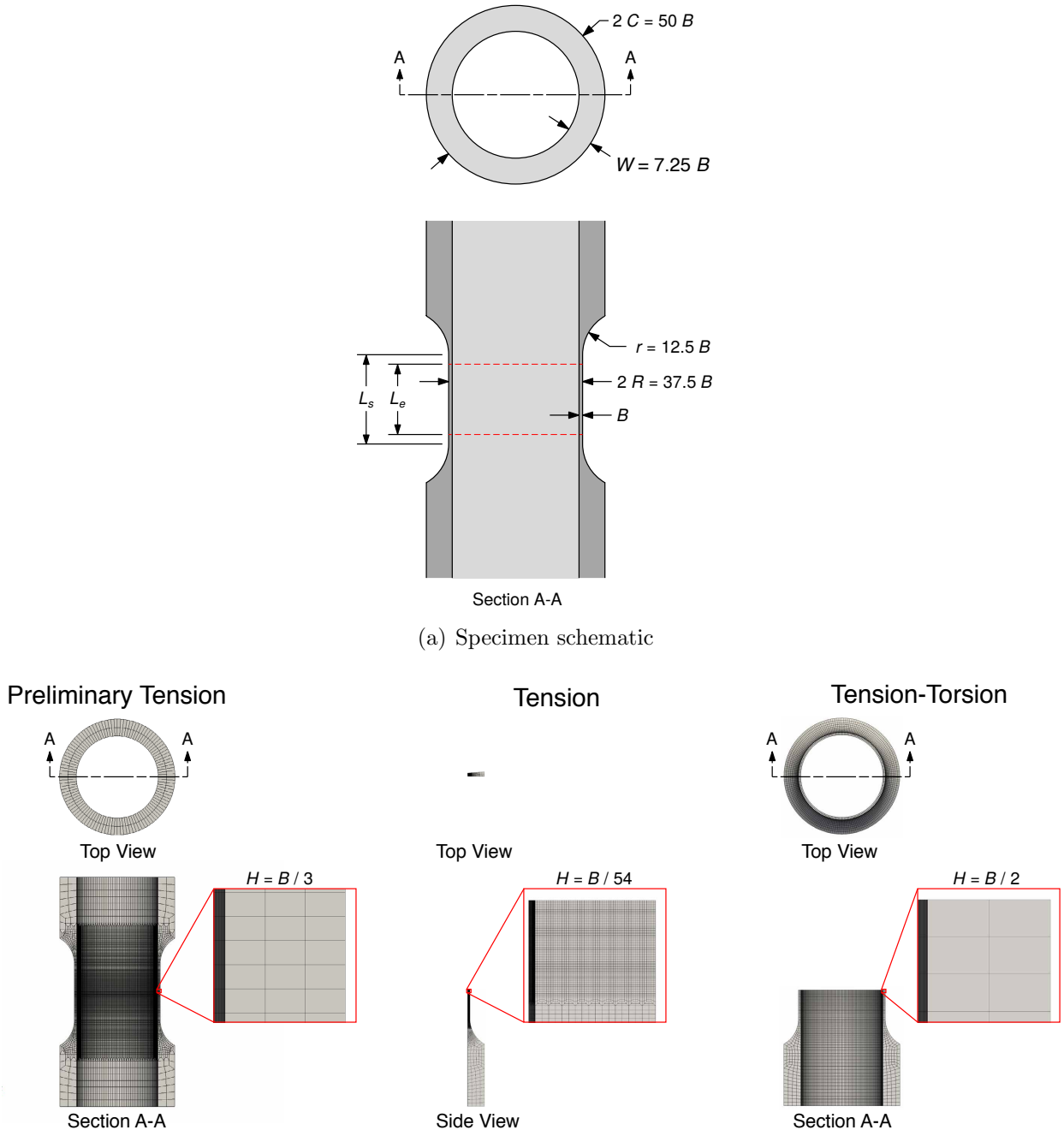

(a) Specimen schematic

(b) FE meshes

Figure B.1. Smooth tube specimen geometry and finite element meshes. The extensometer gage length in (a) is shown at its assumed value of $L_e = 10$ mm.

smooth tube and smooth bar responses, as well as four simulations with different smooth lengths. The first smooth length $L_s = 12.7$ mm corresponds to the experiment, while

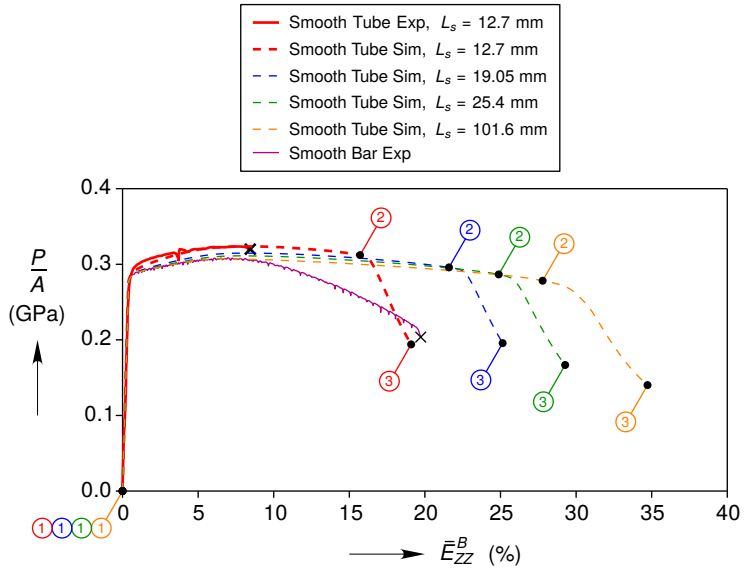

Figure B.2. Smooth tube and smooth bar tension experiments compared against smooth tube simulations with various thin wall section gage lengths.

$L_s = 19.05$ mm, 25.4 mm, and 101.6 mm are 1.5×, 2×, and 8× longer than the experiment. The extensometer gage length remained 10 mm for all simulations. The responses are plotted as Biot stress P/A versus the Biot strain E^B_{ZZ}, which are equivalent to engineering stress and engineering strain, respectively, for principal deformations[1]. Note that the smooth tube response measurement slightly exceeds the smooth bar response measurement at the onset of yield. The smooth tube and smooth bar responses prior to maximum load are reasonably captured by the $L_s = 12.7$ mm and $L_s = 101.6$ mm simulations, which demonstrates that the extensometer gage length in the $L_s = 12.7$ smooth tube is not in a state of uniaxial stress. The lateral contraction of the smooth thin wall section is constrained near the thick shoulders ($W = 7.25B$), which leads to a hoop stress inside the extensometer gage length if L_s is sufficiently short. The smooth thin wall length also has an interesting effect on the necking behavior, as shown in the ε^p_e field images in Fig. B.3(c), which correspond to the circled number instances in Fig. B.2. After the maximum load, the tube outer diameter necks inward, but eventually the simulation predicts necking across the wall thickness. Small values of L_s give an axisymmetric neck, while large values of L_s produce a criss-crossing pattern of high strain similar to the experimental observations in Fig. B.3(a) and (b). Obviously, L_s had to be artificially increased to induce the criss-crossing, but this result shows that the instability is not outside of the realm of possibility. Perhaps a different material model would produce criss-crossing in the actual smooth length of $L_s = 12.7$ mm. For now, however, the thin wedge (Fig. B.1(b)) with axisymmetric boundary conditions is a legitimate approach to

[1]If an anisotropic material's principal axes are not aligned with the uniaxial loading axis, it is possible to induce non-principal deformations that cause the Biot stress and strain to deviate from engineering stress and strain, but that did not occur here.

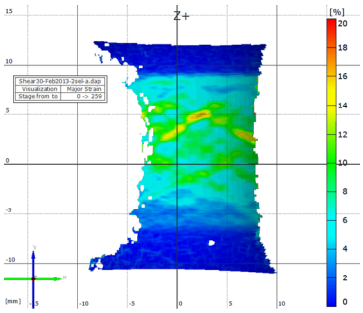

(a) Measured maximum principle strain just prior to failure

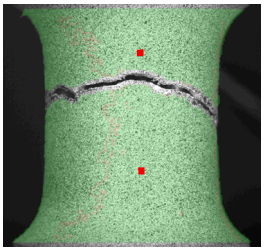

(b) Failed specimen

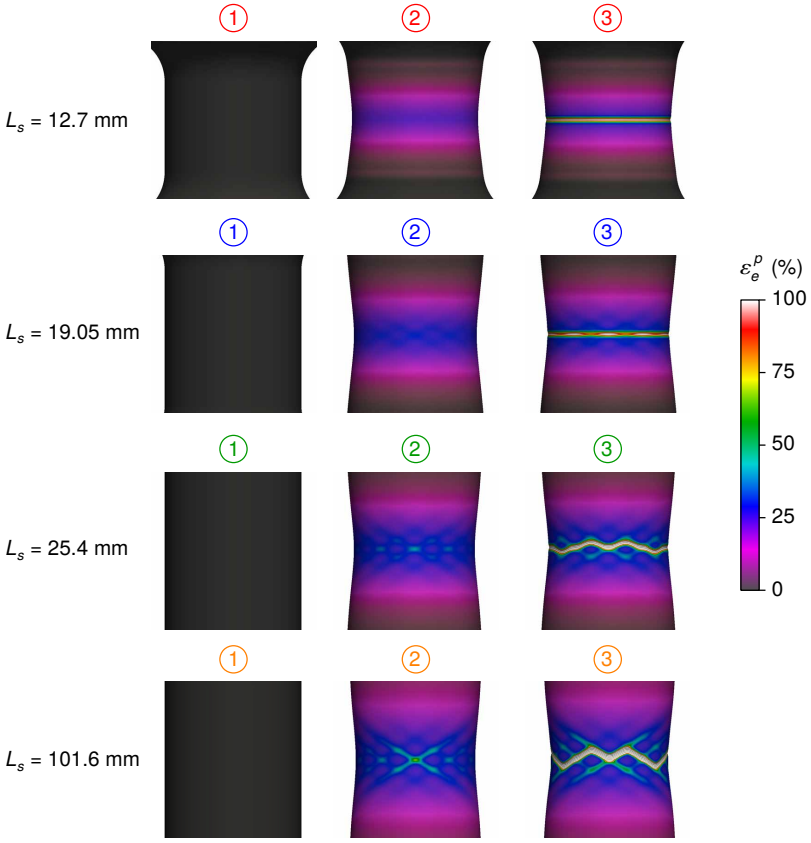

(c) Equivalent plastic strain fields

Figure B.3. A sawtooth pattern of high strain was observed in the smooth tube tension experiment, and the subsequent crack followed the same pattern. When the experimental specimen is faithfully modeled, with a smooth length of $L_s = 12.7$ mm, the simulation predicts a circular ring of high strain. When the smooth length is increased beyond the actual experimental specimen length, the high strain region transitions into a sawtooth pattern.

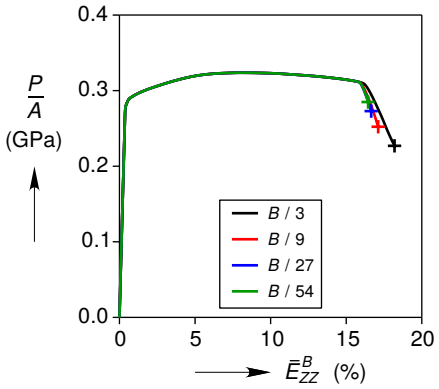

Figure B.4. Mesh convergence of the smooth tube mechanical response and failure under tension.

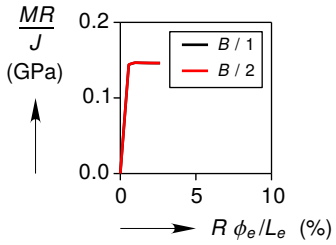

Figure B.5. Mesh convergence of the smooth tube mechanical response under combined tension-torsion.

simulate the smooth tube tension experiment.

The mesh convergence of the tension boundary value problem and the tension-torsion boundary value problem are shown in Fig. B.4 and Fig. B.5, respectively. In tension, we considered the convergence of the mechanical response as well as the failure prediction. The mechanical response prior to the through thickness necking is well represented by only three elements across the thickness, but 27 elements appear to be needed after the onset of through thickness necking. The failure prediction, on the other hand, has not converged even with 54 elements across B. Further refinement may lead to failure directly after necking, but the onset of necking would remain the same. In tension-torsion, roughly equal amounts of tensile and shear strain were applied, and we only considered convergence of the mechanical response. The vertical axis MR/J in Fig. B.4 is the engineering shear stress, while $R\phi_e/L_e$ is the average engineering shear strain across the extensometer. Two elements across B is sufficient to resolve the torsion and axial (not shown) responses in tension-torsion to the small deformations considered.

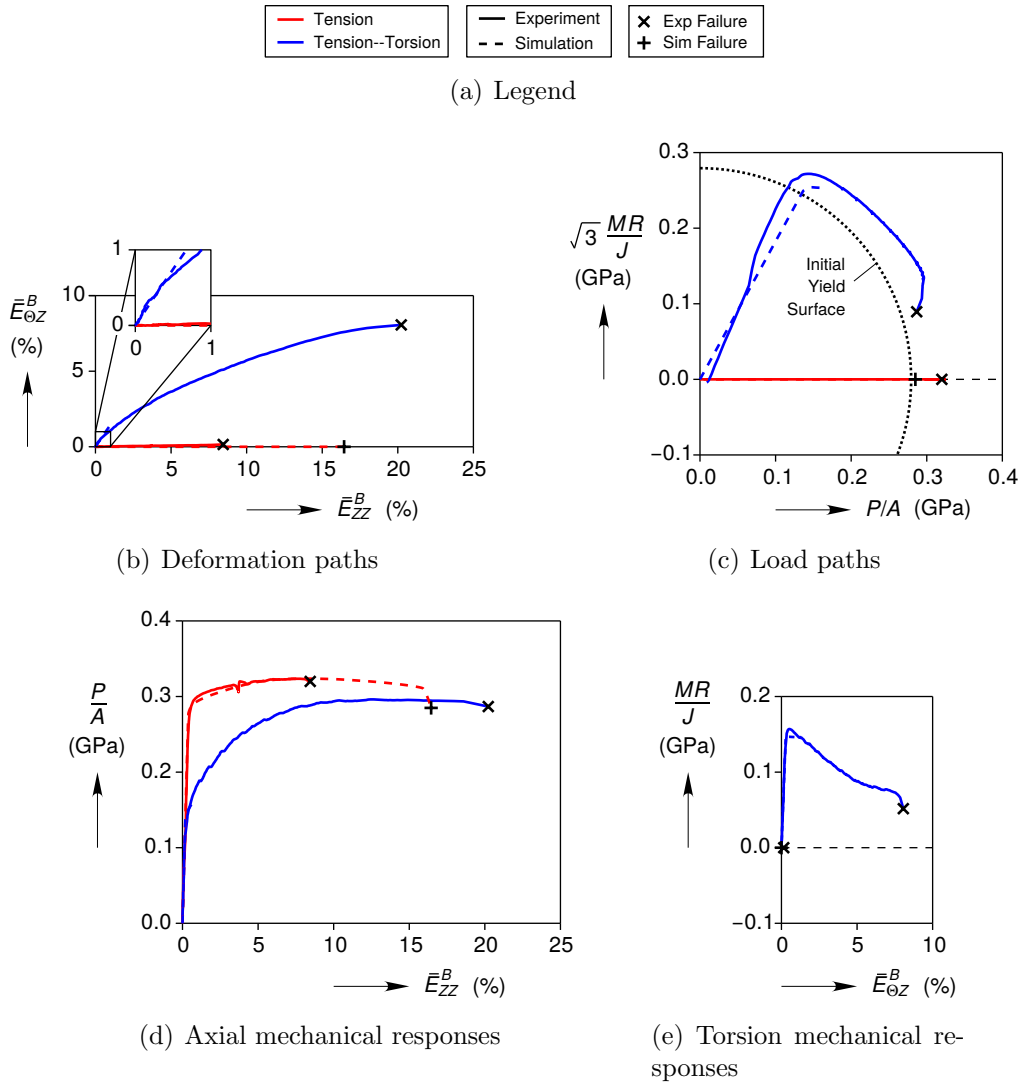

(a) Legend

(b) Deformation paths

(c) Load paths

(d) Axial mechanical responses

(e) Torsion mechanical responses

Figure B.6. Smooth tube experiments compared against simulations.

The smooth tube simulation results are compared against the experiments in Fig. B.6. The experiments are plotted using the Biot shear strain averaged across the extensometer length $\bar{E}^B_{\Theta Z}$, while the simulations are plotted using the engineering tensorial shear strain averaged across the assumed extensometer length $R\phi_e/(2L_e)$. The difference between $\bar{E}^B_{\Theta Z}$ and $R\phi_e/(2L_e)$ should be negligible for the small shear strains simulated. The comparisons between the simulations and the experiments on the smooth tube are similar to the notched tube. The smooth tube tension specimen fails at the maximum load, while the simulation continues well past maximum load before the failure is predicted (see Fig. B.6(d)). The tension-torsion simulation follows a linear path tangent to the initial path measured in the experiment (see Fig. B.6(b)). This linear path was chosen because the initial portion of experimentally measured path determines the initial yield stresses. As shown in Fig. B.6(c)

and (e), the simulation slightly under predicts the shear stress and over predicts the axial stress. Hopefully, future work will show whether these discrepancies are due to non-linearities in the experimental strain path in Fig. B.6(b) or due to anisotropic plasticity.

DISTRIBUTION:

1	MS 0346	M. Neilsen, 1526
1	MS 0346	D. Peebles, 1526
1	MS 0346	J. Holland, 1526
1	MS 0346	R. Teeter, 1526
1	MS 0346	D. Vangoethem, 1526
1	MS 0346	R. Jameson, 1526
1	MS 0557	S. Kramer, 1558
1	MS 0828	G. Orient, 1544
1	MS 0828	K. Hu, 1544
1	MS 0828	W. Witkowski, 1544
1	MS 0840	W. Scherzinger, 1554
1	MS 0840	N. Breivik, 1554
1	MS 0840	T. Hinnerichs, 1554
1	MS 0840	C. Lo, 1554
1	MS 0840	J. Bean, 1554
1	MS 0840	E. Corona, 1554
1	MS 0840	J. Bishop, 1554
1	MS 0840	S. Grange, 1554
1	MS 0840	K. Gwinn, 1554
1	MS 0840	E. Fang, 1554
1	MS 0840	J. Pott, 1555
1	MS 0840	M. Bailey, 1555
1	MS 0840	J. Koester, 1555
1	MS 0845	M. Tupek, 1542
1	MS 1135	D. Epp, 1531
1	MS 9042	M. Chiesa, 8259
1	MS 9042	B. Antoun, 8256
1	MS 9042	W.-Y. Lu, 8256
1	MS 9042	J. Ostien, 8256
1	MS 9957	H. Jin, 8256
1	MS 0899	Technical Library, 9536 (electronic copy)


Sandia National Laboratories